Production of elastin-like recombinamer-based nanoparticles for Docetaxel encapsulation and use as smart drug-delivery systems using a supercritical anti-solvent process

R. Vallejo[a,b], J. Gonzalez-Valdivieso[b], M. Santos[b], S. Rodriguez-Rojo[a*], F. J. Arias[b*]

[a] BioEcoUVa, Research Institute on Bioeconomy, High Pressure Process Group, University of Valladolid, Department of Chemical Engineering and Environmental Technology, Escuela de Ingenierías Industriales, Sede Mergelina, 47011 Valladolid, Spain

[b] BIOFORGE Research Group, University of Valladolid, CIBER-BBN, LUCIA Building, Paseo Belén 19, 47011 Valladolid, Spain

* Corresponding authors:

arias@bioforge.uva.es

soraya.rodriguez@uva.es

ABSTRACT

This study presents a new groundbreaking methodology for integrating innovative concepts to develop novel drug delivery strategies. This methodology combines genetically engineered elastin-like recombinamers (ELRs) with supercritical fluid (SCF) techniques to encapsulate a poorly water-soluble drug in a one-step process. The chemotherapeutic agent Docetaxel (DTX) is encapsulated with a block copolymer ELR containing the RGD peptide, a specific target sequence for cancer cells, using the supercritical anti-solvent (SAS) technique in a high process yield of up to 70%. SEM studies show spherical microparticles of 10 µm after encapsulation. After dispersion under physiological conditions, microparticles disaggregate into stable monodisperse

nanoparticles of 40 nm size and -30 mV ζ-potential. This protects the drug, as confirmed by NMR analysis, thereby increasing the water solubility of DTX up to fifty orders of magnitude. The delivery process is governed by the Fick diffusion mechanism and indicates that the presence of DTX on the particles surface is practically negligible. Cellular assays showed that, due to the presence of the cancer target sequence RGD, breast cancer cells were more affected than human endothelial cells, thus meaning that the strategy developed in this work opens the way to new controlled release systems more precise than non-selective chemotherapeutic drugs.

KEYWORDS

Elastin-like recombinamers (ELRs); supercritical anti-solvent (SAS); docetaxel; drug delivery; cancer therapy;

1. INTRODUCTION

The development of advanced materials that improve currently available biomedical devices is a challenge in all fields of technology [1]. Excellent candidates for these applications include protein-based biopolymers inspired by naturally occurring proteins from the extracellular matrix (ECM). Of these, elastin has properties that make it unique in this field [2], and various studies in recent years have focused on the development of so-called elastin-like recombinamers (ELRs) [3-5]. These recombinant biopolymers, inspired by natural elastin, contain the sequence of repeating units (Valine-Proline-Glycine-X-Glycine: VPGXG)$_n$, where X can be any amino acid except proline, due to steric hindrance when the transition occurs. ELRs preserve the unique mechanical properties found in elastin (extraordinary elasticity, ability to self-assemble and excellent resistance to stress), includingexcellent and biocompatibility and interesting bioactivity.

The application of ELRs in ~~the field of~~ biomedicine is increasing [3, 5] ~~due~~thanks to the~~ir~~ significant advantages: (1) ~~that they present, especially as~~ genetic engineering allows total control ~~over~~of their architecture and design, and (2) ~~as well as the~~ ability to create ~~monodisperse~~ polymers with higher complexity compared to those chemically synthetized ~~ones a complexity that is far greater than for those synthesized chemically~~. Moreover, both their natural ability to self-assemble and stimuli responsiveness allow the production of smart and complex systems [6]. Furthermore, their manufacture is easily scalable [7]. The smart nature of ELRs resides in their characteristic inverse temperature transition (ITT) [8]. Thus, below a specific temperature, known as the transition temperature (Tt), the ELR chains are hydrophobically hydrated, forming a disordered state of random coils [9], whereas above Tt the structure loses its water molecules to form a phase-separated state in which the ELRs adopt a dynamic, regular, and ordered β-spiral structure, thereby resulting in a variation in enthalpy. This folding is reversible if the temperature is decreased below Tt [10].

ELRs have been shown to allow the controlled release of highly hydrophobic drugs that are difficult to dispense [11] in different ways, such as topical or intravenous [12-15]. Of the many different ELR-based advanced drug-delivery devices available, nanoparticulate delivery systems present great advantages since they allow a wide range of administration routes (oral, parenteral, transdermal, nasal, ocular, etc.) [16, 17]. However, difficulties still exist when formulating protein-based nanoparticle systems, for example in cases where the use of organic solvents, which may be toxic, requires an additional step to remove them, or when the encapsulation efficiencies are low [18, 19]. The use of supercritical fluids (SCF), which is any substance at a temperature and pressure above its critical point, is a viable option to consider when producing micro- or nanoparticulate

systems for controlled drug release. SCF technologies, especially those involving supercritical carbon dioxide (scCO$_2$), have been studied as sustainable alternatives for polymer processing. Thanks to the moderate temperature and pressure at which the supercritical state is reached (~~73.8 bar~~7.38 MPa and 33.1°C), scCO$_2$ allows polymers to be processed at low temperatures, generally below 50°C, and under an inert atmosphere that is non-flammable, non-corrosive, non-toxic and non-carcinogenic. Further, scCO$_2$ does not generate waste since it can be recycled, and is an excellent green solvent due to its solvent strength [20-23]. The advantages offered by methods that use scCO$_2$ for the micronization of particle (either as a solvent or anti-solvent) compared to traditional methods that involve organic solvents include better control of particle size and morphology and a narrow particle-size distribution [24-26]. One of the most versatile processes for the formation of particles with scCO$_2$ is the process known as supercritical anti-solvent (SAS) [27], in which scCO$_2$ acts as an anti-solvent, extracting the organic solvent and hence decreasing the solubility of the solutes in the mixture, which results in a rapid supersaturation and the nucleation and formation of nano- or microparticles. The particle size and morphology of the particles can be controlled by adjusting the process parameters, including scCO$_2$ density, which depends on temperature and pressure, solution concentration, nozzle geometry and flow rate. The Supercritical Antisolvent technique has been widely used for the precipitation and encapsulation of pharmaceutical compounds as recently reviewed [28]. Some examples found in the literature about drug encapsulation with supercritical fluids involve polymers whose mechanical and biological properties are far from the ELRs, as encapsulation of ibuprofen or antioxidants with poly(l-lactic acid), EUDRAGIT L100® or polycaprolactone, among others [29-32]. The novelty of the technique described in this manuscript lies in the use of protein-based biopolymers designed by genetic engineering as encapsulating agents. In this sense, to

our knowledge, the literature only offers one result about impregnation of ELRs at high pressures with CO_2 [33] but no results about SAS and elastin-like recombinamers (ELRs). Therefore, the combination of recombinant elastin-like biopolymers with the SAS technique is a field to explore and becomes a new method of application for encapsulating active agents. In addition, economic studies support the use of SCF, specifically $scCO_2$, thus contributing to its increasing use by the food and pharmaceutical industries [28].

In recent years, the encapsulation of docetaxel (DTX) has been the subject of study by many researchers [34-37] due to its poor solubility in water (0.013 mg/mL) [38]. Indeed, many groups have designed long and complex methods that also commonly involve the use of toxic organic solvents such as dichloromethane or have low encapsulation efficiencies [39-41]. In this paper, we demonstrate the encapsulation and *in vitro* evaluation, of an especially hydrophobic drug, namely DTX, with a bioactive and biocompatible ELR biopolymer; thus isolating the compound, avoiding side effects and allowing the release of appropriate quantities in the specific regions where the therapeutic dose is needed. To that end, we take advantage of an eco-friendly process, namely the SAS process, in order to obtain a nanoparticulate drug-delivery system in a one-step process.

2. MATERIALS AND METHODS

2.1 Materials

Dimethyl sulfoxide (DMSO) was purchased from Sigma Aldrich with a purity of ≥99.7%. Carbon dioxide was supplied by Carburos Metálicos S.A. with a purity of 99.95%. Docetaxel (DTX) was provided by Apollo Scientific with a purity of 99%. Deuterium oxide was purchased from Sigma Aldrich with a purity of 99.9 atom % D. Fetal bovine

126 serum (FBS), penicillin/streptomycin solution, trypsin-EDTA, DPBS, and LIVE/DEAD®

127 Viability/Cytotoxicity Kit for mammalian cells were supplied by Invitrogen (USA).

128 Human umbilical vein endothelial cells (HUVEC cc-2517), medium 200, low serum

129 growth supplement (LSGS), L-15 medium and gentamicin/amphotericin solution were

130 purchased from Gibco. The human breast cancer MDA-MB-231 cell line (86010202

131 ECACC) was supplied by Sigma-Aldrich.

132

133 *2.1.1 Elastin-like recombinamers*

134 (EI)x2 and (EI)x2RGD were constructed using standard genetic-engineering techniques

135 and purified by Inverse Transition Cycling (ITC), with several cycles of precipitation

136 (heating) and resuspension of the supernatant (cooling), as described by Meyer *et al*. [42].

137 The final product obtained was dialyzed against deionized water and freeze-dried

138 before~~prior to~~ storage.

139

140 (EI)x2 is a 92.896 KDa polymer and consists on a tetrablock design involving two

141 hydrophilic blocks containing glutamic acid (**E**) and two hydrophobic blocks containing

142 isoleucine (**I**) as guest residues (Figure S1). Its aminoacid sequence is MESLLP-

143 [[(VPGVG)$_2$ VPG**E**G (VPGVG)$_2$]$_{10}$-(VG**I**PG)$_{60}$]$_2$-V.

144

145 (EI)x2RGD is a 112.270 KDa polymer and consists on a tetrablock design involving two

146 hydrophilic blocks containing glutamic acid (**E**) and two hydrophobic blocks containing

147 isoleucine (**I**) as guest residues (Figure S1). (EI)x2RGD also includes the **RGD** peptide,

148 a specific target sequence for cancer cells. Its aminoacid sequence is MESLLP-

149 [(VPGVG)$_2$ VPG**E**G(VPGVG)$_2$]$_{10}$-(VG**I**PG)$_{60}$]$_2$-VG-[(VPG**I**G)$_{10}$-AVTG**RGD**SPASS-

150 (VPG**I**G)$_{10}$]$_2$-V.

151   ~~(EI)x2 sequence: MESLLP [[(VPGVG)$_2$ VPGEG (VPGVG)$_2$]$_{10}$ (VGIPG)$_{60}$]$_2$ V~~

152   ~~(EI)x2 Molecular Weight: 92,896 Da.~~[43, 44].

153

154   The biopolymers contain two different functional blocks to achieve an adequate balance

155   between biocompatibility and mechanical and thermal responses. (EI)x2RGD contains

156   two repetitions of a peptide loop found in the human fibronectin protein with the well-

157   known RGD sequence for cancer cell targeting.

158

159   The physicochemical properties of the ELRs can be modulated by choosing the amino

160   acid in the X position as guest residue. Self-assembling of amphiphilic di-block

161   copolymers result in the formation of aggregates composed by a core formed by the

162   insoluble block, which is shielded from the solvent by a hydrated corona formed by the

163   more soluble block. The γ-carboxylic groups from the glutamic acid residues (pKa 4.1)

164   displayed on the hydrated corona of the nanoparticles should be on the deprotonated state

165   at pH 7.4. Therefore, glutamic acid is responsible for the pH-responsiveness.

166

167   Furthermore, Urry deeply studied the thermoresponsive behavior of ELRs and

168   determined the different transition temperatures for each one of the aminoacids at the

169   guest position (X) within the VPGXG pentapeptide [45]. Regarding the thermoresponsive

170   behavior of (EI)x2 and (EI)x2RGD polymers, thermoresponsiveness is mainly due to the

171   isoleucine-containing block, since this pentapeptide was demonstrated to self-assemble

172   at 15°C. Contrary, the ELR block involving glutamic acid self-assembles above 70°C.

173   Thus, self-assembling of both (EI)x2 and (EI)x2RGD polymers under physiological

174   conditions (37°C) is only due to the isoleucine-containing block as the block containing

175   glutamic acid remains in soluble state.

176

2.2 Methods

2.2.1 Supercritical antisolvent process

A schematic representation of the supercritical antisolvent process pilot plant, and its modifications (striped lines), used to encapsulate docetaxel in ELRs is shown in Figure 1. Briefly, $scCO_2$ was continuously pumped (2) into the precipitation vessel (6) at a flow rate of 2 kg/h at the corresponding operating pressure and temperature. Once a steady state had been achieved, a defined quantity of ELR and DTX dissolved in DMSO (5) was pumped through a nozzle into the precipitation chamber (6) at a flow rate of 0.5 mL/min. After drying the particles with fresh CO_2 ~~in order~~ to remove residual solvent, they were recovered from the porous metal filter (7), with a screen size of 1 μm, placed outside the precipitator vessel. A detailed description of the equipment can be found in Natolino *et al*. [46]

The procedure was optimiszed with (EI)x2 ELR (400 mg in each experiment) to determine the appropriate nozzle design (coaxial or non-coaxial; Figure S2) and drying process, thus minimizing the DMSO residue and enhancing the process yield. The influence of pressure (9.5-11.0 MPa) and ELR concentration (15-40 mg/mL of (EI)x2) was also studied. Three drying methods were employed. In method 1, particles were dried in the reactor at 2 kg/h $scCO_2$ mass flow for 2 h; in method 2, a bypass line was implemented (figure 1 dashed lines) and the particles kept in the filter were dried for 15 min at 2 kg/h scCO2 mass flow; and in method 3, the reactor was flushed for 45 min at 2 kg/h scCO2 mass flow, and then the particles retained by the filter were dried for 15 min at the same scCO2 mass flow.

200

201
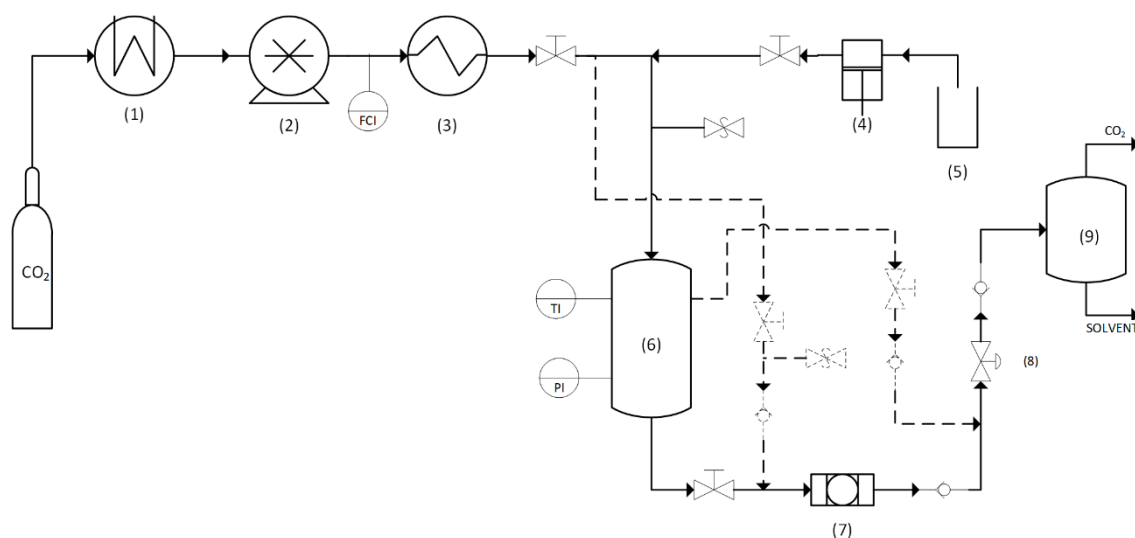
Figure 1. Schematic flow diagram of the SAS pilot plant. (1) cooler, (2) CO_2 pump, (3)
heater, (4) chromatographic pump, (5) solution, (6) precipitator vessel, (7) filter, (8) back-
pressure valve, (9) separator. Striped lines represent the bypass modification implemented
in the pilot plant.

2.2.2 Product characterization

The proportions of ELR:DMSO and ELR:DMSO:DTX were determined by nuclear

magnetic resonance (NMR) using samples prepared in D_2O or DMSO-d6, respectively,

at 1 mg/mL. Spectra were recorded using a 400 MHz Agilent spectrometer (Laboratory

of Instrumental Techniques, University of Valladolid) with a 1 s relaxation delay between

transients, 45° pulse width, 512 transients per sample and a spectral width of 6410 Hz for

DMSO-d6, and 8012 Hz for D_2O. Proportions were obtained by comparing the integral

of the signal for the methyl groups from the ELR with those of the methyl groups of

DMSO when the spectrum is recorded in D_2O. The spectrum in DMSO allows a

comparison between the methyl groups from the ELR and those for the protons of the

aryl moieties of DTX.

NMR was also used to analyze the behavior of the pure ELR and the encapsulated DTX

as a function of temperature. In this case, a 500 MHz NMR Agilent DD2 instrument

221 equipped with a cold probe was used. NMR spectra recorded report ^{1}H chemical shifts

222 (δ) in parts per million (ppm) and are referenced to tetramethylsilane (TMS), using the

223 residual solvent peak as an internal reference. The NMR samples (1 mg/mL) were

224 dissolved in 650 μL of D_2O for internal lock and then transferred into a 5 mm NMR tube.

225 The acquisition parameters used to obtain quantitative ^{1}H spectra were as follows: 10 s

226 relaxation delay between transients, 45° pulse width, spectral width of 8012 Hz, a total of

227 16 transients and acquisition time of 2.044 s. All spectra were analyzed using MestreNova

228 v 9.0.1.

229

230 Particle morphology was studied by scanning electron microscopy (SEM) at the

231 Advanced Microscopy Laboratory (Laboratory of Instrumental Techniques, University

232 of Valladolid) using an ESEM QUANTA 200 FEG instrument. The powder obtained after

233 SAS process of representative samples wasere placed under an argon atmosphere at room

234 temperature beforeprior to examination at two different magnifications (500x and 5000x)

235 for comparison. The voltage used in each SEM analysis was 1 kV, which provided a

236 sufficient resolution and did not produce any changes in the samples. The particles in the

237 photomicrographs were measured using a Carl Zeiss GmbH microscope and the 2011

238 ZEN 2.3 (blue edition) software. More than 300 particles were measured in each

239 experiment to determine mean particle size as D(0.5) and standard deviation.

240

241 The transition temperature was measured by differential scanning calorimetry (DSC)

242 using a Mettler Toledo 822e (USA) instrument with a liquid-nitrogen cooler. Samples

243 were dissolved overnight (O/N) at 50 mg/mL and pH 7 in ultrapure deionized water below

244 Tt (4°C) The heating program for DSC experiments included an initial isothermal stage

245   (5 min at 0°C for stabilization of the temperature), followed by heating at 5°C/min from

246   0 to 60°C.

247

248   Surface charge (ζ-Potential) and size in aqueous solution were measured by dynamic light

249   scattering (DLS) using a Zetasizer Nano ZS (Malvern Instruments Ltd., UK). Pure ELR

250   samples were dissolved at 1 mg/mL in ultrapure deionized water below Tt (4°C) O/N,

251   then the temperature was raised above Tt at 37°C for 15 min. Samples were adjusted to

252   neutral pH with NaOH 0.5 M at room temperature and filtered through a 0.45 µm nylon

253   filter to avoid the presence of dust. ELRs with encapsulated DTX were dispersed at 1

254   mg/mL and 37°C using a vortex, and then the same procedure described previously was

255   followed. Three measurements were taken per sample.

256

257   Particle morphology and the amphiphilic behavior of the biopolymer in aqueous media

258   were observed by TEM using a JEOL JEM-1230 instrument equipped with an Orius

259   SC1000 (4008×2672 pixels) cooled slow-scan CCD camera (GATAN, UK) (Bilbao,

260   Spain). Samples were prepared at a concentration of 1 mg/mL in ultrapure deionized

261   water with negative staining at neutral pH and room temperature. The particles in the

262   photomicrographs were measured using a Carl Zeiss GmbH microscope and the 2011

263   ZEN 2.3 (blue edition) software. More than 500 particles were measured to determine

264   particle size as D(0.5) and standard deviation.

265

266   *2.2.3.- In vitro release studies*

267   *2.2.3.1. Experimental procedure to acquire the drug-delivery profiles*

268   *In vitro* drug-delivery experiments containing DTX formulations usually involve

269   mixtures with polysorbate 80. Since surfactants could affect the amphiphilic behavior of

the ELR in aqueous solution, the assays were performed in triplicate at 37°C by using the dialysis method and avoiding the use of surfactants as described elsewhere [47], by dispersing 1 mg of (EI)x2+DTX particles in 1 mL of 7:3 (v/v) water/ethanol release medium containing 0.6 mg of encapsulated DTX. Previously activated dialysis bags (MWCO 12,000 kD) were filled with this solution and sealed at both ends. These bags were then immersed in 30 mL glass vials, previously filled with 20 mL of release medium. The content of these vials was stirred at 80 rpm and 37°C in an incubator throughout the experiment. A 2 mL sample was withdrawn from the release medium at predetermined time intervals and the same volume of fresh medium added to maintain sink conditions. As a control, the drug delivery assay was carried out with pure DTX (0.6 mg), also in triplicate.

The amount of DTX released with time was determined by UV-vis spectrometry (UV-Vis NanoDrop 2000, Thermo Scientific) following the Lambert-Beer law, at a wavelength of 234 nm. A calibration curve was plotted beforehand using solutions of DTX dissolved in a 7:3 (v/v) water/ethanol at a concentration of between 62.5·and 0.98·µg/mL.

2.2.3.2. Description of the mathematical models

To analyze the kinetics of the DTX release profiles and the mechanisms assigned to the delivery process, release profiles were studied using two mathematical models, as described below.

The Lindner and Lippold equation describes the release through a polymeric matrix. In this equation, *n* takes different values for different geometries and release mechanisms,

295 k_1 represents the Fickian diffusion constant, and a parameter 'b' is included to represent

296 the burst effect

297

$$\frac{M_t}{M_\infty} = k_1 \cdot t^n + b \tag{1}$$

298

299 The biexponential Peppas–Sahlin equation was also used to determine the contribution of

300 the Fick diffusion process and relaxation of the polymer chains irrespective of the

301 geometry of the release system. In this equation, n has the same meaning as in equation

302 (1), k_1 represents the Fickian diffusion constant and k_2 represents the polymer chain

303 relaxation constant.

304

$$\frac{M_t}{M_\infty} = k_1 \cdot t^n + k_2 \cdot t^{2n} \tag{2}$$

305

306 *2.2.4 Cell-based assays*

307 *2.2.4.1 Cell culture*

308 HUVEC cells were grown in Medium 200 supplemented with 1%

309 gentamicin/amphotericin and LSGS at 5% CO_2 and 37°C. MDA-MB-231 cells were

310 cultured in L-15 medium supplemented with 10% FBS, 100 U/mL penicillin and 0.1

311 mg/mL streptomycin at 0% CO_2 and 37°C. When required, cells were detached using a

312 solution of 0.05% Trypsin-EDTA. Cells were seeded onto 96-well plates in a quantity of

313 2×10^4 cells per cm^2 for tumour cells and 1×10^4 cells per cm^2 for primary cells, in order to

314 maintain the same confluence levels for both cell lines overnight before treatment.

315

316 *2.2.4.2 Fluorescence microscopy*

317   MDA-MB-231 cells were seeded and, after 24 hours, incubated with rhodamine-loaded

318   nanoparticles ((EI)x2RGD+Rho produced using the SAS process) for 2 hours. Cells were

319   then washed with PBS 1X, fixed with PFA 4% and permeabilized with Triton 0.1%. Cell

320   nuclei were stained with DAPI. Fluorescence images were taken using a Nikon eclipse

321   Ti-SR (Japan) fluorescence microscope.

322

323   *2.2.4.3 Confocal microscopy*

324   MDA-MB-231 cells were seeded and, after 24 hours, incubated with rhodamine-loaded

325   nanoparticles ((EI)x2RGD+Rho produced using the SAS process) for 2 hours. Cells were

326   then washed with PBS 1X, fixed with PFA 4% and permeabilized with Triton 0.1%. Cell

327   nuclei were stained with DAPI. Images were taken using a Leica TCS SP8 X confocal

328   microscope at the Laboratory of Instrumental Techniques (University of Valladolid).

329

330   *2.2.4.3 Cell viability*

331   HUVEC and MDA-MB-231 cells were treated for 24 hours with free DTX at three

332   concentrations (0.1, 1 and 10 µM) or different ELR-based nanoparticles (lacking or

333   containing DTX) at normalized concentrations, as indicated (Table S2).

334

335   The LIVE/DEAD Viability/Cytotoxicity Assay Kit (Invitrogen) was used according to

336   the manufacturer's instructions. Briefly, a stock solution of the LIVE/DEAD reagents (1

337   µM calcein AM and 2 µM EthD-1 in DPBS) was added to the samples and, after

338   incubation for 20 minutes in the dark, the fluorescence intensity emission was measured

339   at 525 and 645 nm (SpectraMax M5e Molecular Devices microplate reader).

340   Additionally, images of cell cultures were taken using a Nikon eclipse Ti-SR (Japan)

341   fluorescence microscope. Three independent experiments were performed in triplicate.

342

2.2.4.4 Cell proliferation

MDA-MB-231 cells were seeded in 96-well plates. After incubation for 24 hours, cells

were treated with free 1 µM DTX or DTX-loaded nanoparticles at an equivalent

concentration for 72 hours. Confluence percentages were determined every 4 hours using

the Cytosmart OMNI (Cytosmart, Netherlands) [6]. Results are provided as the cellular

confluence of the wells. Three independent experiments were performed in triplicate.

2.2.4.5 Statistical analysis

Data are reported as mean $\pm$ SD (n = 3). Statistical analysis involved variance analysis in

combination with a subsequent analysis using the Bonferroni method. A p-value of less

than 0.05 was considered to be statistically significant. *$p < 0.05$, **$p < 0.01$, ***$p <$

0.001. Data were handled using the SPSS Statistics software version 20 (IBM).

3. RESULTS AND DISCUSSION

3.1 Optimization of the supercritical antisolvent process (SAS)

The healing potential and benefits of DTX mean that this drug is widely used in cancer

therapy. ~~However, conventional DTX treatment presents disadvantages, such as the form of administration and the presence of alcohol, which can cause intoxication, thus meaning that new release systems are essential.~~ However, conventional DTX treatment [48]

presents disadvantages, such as the form of administration or the use of non-ionic

surfactant vehicles for their formulation, which can alter the pharmacokinetics of the

drugs thereby predisposing them to greater toxicity [49]. For this reason, new release

systems are needed. In this regard, the use of ELRs has been selected as a candidate to

366 protect, direct and release the drug in a controlled manner ~~in order~~ to avoid unwanted side

367 effects.

368

369 ELRs were used initially in the SAS process to obtain microparticles. Thus, screening

370 experiments with the (EI)x2 biopolymer were carried out ~~in order~~ to determine the

371 optimal operating conditions. DMSO was chosen as the solvent because of the high

372 solubility of both the biopolymer and the drug in it. Furthermore, DMSO is a class 3

373 residual solvent with low toxic potential and no health-based exposure limits according

374 to the European Medicines Agency (EMA) guidelines [50].

375

376 The ELR concentration was fixed originally at 30 mg/mL and the operating temperature

377 was established as 35°C since this moderate temperature does not induce thermal

378 degradation and is above the transition temperature for the ELR, in addition to being easy

379 to reach and maintain. In the initial experiments (1-6, Table 1), the pressure was fixed at

380 ~~110 bar~~11 MPa ~~in order~~ to remain in the single-phase area according to the DMSO:scCO$_2$

381 solubility diagram [41]. The effect of using a simple or co-axial nozzle, as described in

382 Supporting Information Figure S2, was analy~~s~~zed in experiments 1 and 2 under the

383 conditions of drying method 1, as described in section 2.2.1 of the Materials and Methods

384 section. Thus, the use of the new coaxial nozzle results in a decrease in the amount of

385 residual DMSO from 16% to 6%, as well as an increase in the yield from 39% to 56%.

386 This could be explained because~~is due to the fact that~~ the coaxial nozzle enhances

387 spraying by generating smaller droplets, thereby improving the mass transfer between

388 scCO$_2$ and the solution and meaning that supersaturation is greater and is reached faster

389 and more evenly.

390

391 ~~In order t~~To reduce the amount of residual DMSO as much as possible, an improvement

392 in the pilot plant was done in experiment 3 by including a new stream (dotted line in

393 Figure 1) to dry the precipitated powder retained by the filter with fresh $scCO_2$ according

394 to method 2, as described in section 2.2.1. The amount of DMSO was reduced to 1%,

395 although the process yield was seriously compromised. This may be because most of the

396 particles were not dragged down during the process and were not retained by the filter as

397 expected. To solve this problem, experiment 4 included a step of flushing the reactor with

398 fresh scCO2 after pumping the solution (drying method 3, section 2.2.1). As can be seen

399 from Table 1, residual DMSO only increased to 2.4% and the process yield was not

400 compromised, as found for experiment 3. After considering these results, and ~~with the~~

401 ~~intention of~~to study~~ing~~ the repeatability of the process, experiments 1, 2 and 4 were

402 performed in triplicate. As can be seen from Table 1, in terms of yield, the results show

403 good reproducibility, with deviations of less than 3% when the coaxial nozzle was

404 employed. However, the deviation for the residual DMSO content in experiment 4 is high

405 (50%), although the maximum DMSO content is well below that achieved with

406 experiment 2.

407

408 ~~In order t~~To check the effect of ELR concentration on the process, experiments 5 and 6

409 (method 3), in which less concentrated and more concentrated solutions were studied,

410 respectively, were performed. As shown in~~can be seen from~~ Table 1, values are not

411 different taking into account the deviation of the measurements~~the percentage residual~~

412 ~~DMSO was slightly higher in both cases.~~ In the case of experiment 6, a marked decrease

413 in process yield was also observed upon increasing the concentration. The effect of

414 pressure was determined in experiment 7 using the conditions of experiment 4 but

415 operating at ~~95 bar~~9.5 MPa. As can be seen from Table 1, the process yield was lower

than in experiment 4 and the quantity of residual DMSO was higher. This could be
because this operating point is close to the solubility curve of the scCO$_2$-DMSO phase
diagram and the precipitation process is limited by the mass transfer of CO$_2$ into DMSO.
In this case, the supersaturation of the solute is reached slowly, which results in a higher
residual DMSO content. In the case of higher pressure, saturation occurs very rapidly and
mass transfer is enhanced, thus resulting in lower DMSO content [51].

In summary, we can conclude that the best-operating conditions for this process are ~~110 bar~~11 MPa, 35°C, solution concentration of 30 mg/mL, coaxial nozzle and drying method
3 (described previously).

| Exp.	Drying Method	(EI)x2 (mg/mL)	Nozzle Design	Drying Bypass	P (MPa)	DMSO (%)	Yield (%)	Average size (µm)
1	1	30	No coaxial	No	11.0	16.0 ± 1.4	39 ± 6	18 ± 14
2	1	30	Coaxial	No	11.0	6.0 ± 1.0	56 ± 2	n/d
3	2	30	Coaxial	Yes	11.0	1.0	35	n/d
4	3	30	Coaxial	Yes	11.0	2.4 ± 1.2	69 ± 1	10 ± 5
5	3	15	Coaxial	Yes	11.0	3.0	53	13 ± 8
6	3	40	Coaxial	Yes	11.0	3.0	18	10 ± 5
7	3	30	Coaxial	Yes	9.5	3.0	46	9 ± 4

Table 1. Screening experiments to select operating conditions for the SAS process.
Experimental conditions, final DMSO composition (% (w/w)) in the powder obtained
(determined by NMR), average powder size (by SEM) and process yield; n/d: not
determined.

The powder obtained in experiments 1, 4, 5, 6 and 7 was analyzed by SEM. The images
from experiments 1 and 4 can be seen in Figure 2, which shows that the particles produced
during these experiments do not exhibit any marked aggregation and have a smooth

436 surface with many small particles stuck to them, thus resulting in a broad particle-size

437 distribution (Table 1).

438
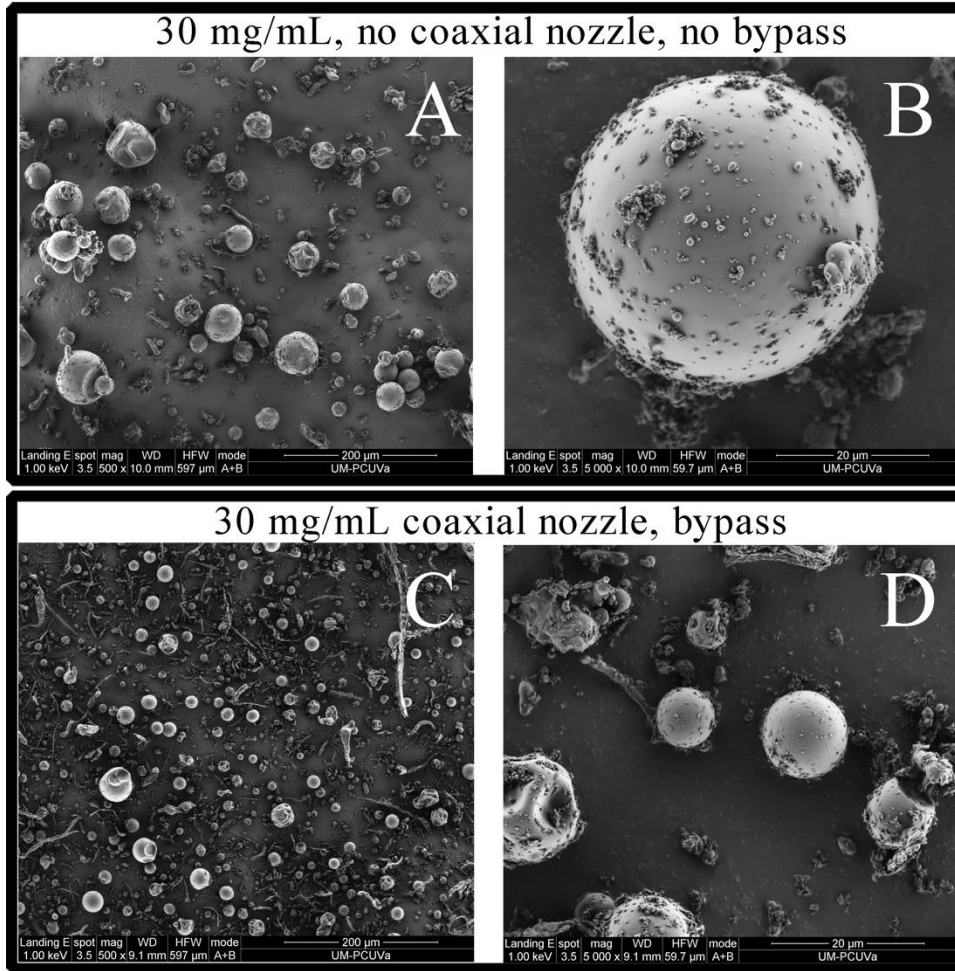
440 **Figure 2**. SEM Photomicrographs showing general (scale bar: 200 µm; magnification:
441 x500; A, C) and detailed views (scale bar: 20 µm; magnification: x5000; B, D) for the
442 powder obtained in experiment 1 (A and B) with no coaxial nozzle and using method 1,
443 and experiment 4 (C and D) with coaxial nozzle and using drying method 3.

444

445 When compared with experiment 4, the only notable changes in particle size and

446 dispersity were observed for the non-coaxial nozzle used in experiment 1 (Table 1, Figure

447 2 A and B). The former produces a smaller particle size and dispersity thanks to the use

448 of the coaxial nozzle, which enhances the spraying homogeneity, thereby producing

449   smaller droplets of the solution inside the reactor and allowing greater mass transfer

450   between the scCO$_2$ and the solvent, thus meaning that supersaturation is greater and is

451   reached faster and more evenly.

452

453   Once the coaxial nozzle and drying method had been established, it was found that, upon

454   decreasing the concentration (experiment 5, table 1, Figure S4 A, B), a higher particle

455   size was found compared with experiments 4 and 6 (Figure S4 C, D). This effect can be

456   explained by the fact that the higher concentration enhances supersaturation, thus causing

457   faster and more homogenous nucleation, which results in a smaller particle size and

458   therefore a more uniform particle size.

459

460   The effect of pressure was analyzed in experiment 7 (Table 1, Figure S4 E, F), with no

461   significant changes in particle size compared with respect to experiment 4 being found

462   even though a decrease in pressure has been reported to produce bigger particles due to a

463   decrease in scCO$_2$ density [52]. Particles with a similar size to those in experiment 4 were

464   found, with an average particle size of 10 µm for the samples produced using the coaxial

465   nozzle and high concentration.

466

467   *3.1.1. Behavior in aqueous solution*

468   The self-assembling nature of ELR molecules in aqueous solution above Tt is governed

469   by the hydrophobic-hydrophilic balance of the block copolymer structure in a bottom-up

470   process, from molecular size to nanosize. Similarly, ELRs from SAS-microparticles

471   should undergo a temperature-driven process to generate particles in aqueous solution.

472   The microparticles obtained after the SAS process (Table 1) were dispersed at 37°C, as

473   described in the Materials and Methods section, and analyszed by dynamic light

474 scattering (DLS; Table 2). The resulting values were then compared with those obtained

475 for the unprocessed (EI)x2, which was solubilized at 4°C and then incubated a 37°C, to

476 determine whether the SAS process has any effect on the behavior of the ELRs.

477

Experiment	D(0.5) (nm)	PDI	ζ-Potential (mV)
1	43 ± 14	0.100 ± 0.009	-34.6 ± 0.4
2	44 ± 18	0.113 ± 0.003	-33.4 ± 0.7
3	51 ± 21	0.147 ± 0.003	-33.1 ± 1.6
4	44 ± 18	0.128 ± 0.005	-34.2 ± 0.8
5	43 ± 14	0.120 ± 0.005	-35.1 ± 1.7
6	40 ± 15	0.134 ± 0.003	-33.6 ± 0.6
7	37 ± 12	0.119 ± 0.004	-32.8 ± 0.4
(EI)x2	41 ± 6	0.030 ± 0.003	-35.4 ± 1.4

478
479 **Table 2.** Values for the diameter D (0.5) and polydispersity index (PDI), determined from

480 the intensity vs. measured size data obtained by DLS, and ζ-potential for samples derived

481 from each experiment described in Table 1. (EI)x2 corresponds to the ELR solution with

482 no SAS processing.

483

484 As shown~~can be seen from~~ in Table 2, the sizes of each sample are quite similar, which

485 implies that the SAS process does not affect the structure or behavior of the polymer in

486 an aqueous medium above Tt, even in the presence of small amounts of DMSO (Table

487 S1). As can be seen from Table 2, aqueous suspensions of the processed particles always

488 produced nearly monodisperse distributions since the PDI value is between 0.1 and 0.7

489 [53] but clearly higher than the value for (EI)x2 without SAS processing (PDI 0.030), this

490 may occurs because the nanoparticle formation process starts from microscale structure

491 and goes from higher to lower scale giving a little more heterogeneous sizes. As such, the

492 process gives better homogeneous associations when ~~starting from the molecular~~

493 ~~dimension~~ the process starts from a molecular structure thereby giving lower PDIs~~than~~

494 ~~when starting from microparticle dispersions~~. Moreover, the ζ-potential results show that

495   ELRs produced using the SAS process have a similar charge to their unprocessed

496   counterparts since scCO$_2$ creates an inert atmosphere that does not interact chemically

497   with the polymer to change its properties. A surface charge higher than -30 mV means

498   that all particles have sufficient charge to form a stable particle system. This fact

499   demonstrates that the process is governed by a hydrophobic-hydrophilic balance of the

500   polymer, with the isoleucine block defining the hydrophobic core and the glutamic acid

501   block defining the corona, which has a negative ζ-potential because of the deprotonated

502   carboxylic group in the side chain.

503

504   To gain~~With the aim of gaining~~ insight into the self-assembling behavior in aqueous

505   medium, a ^{1}H NMR spectroscopic study of SAS-microparticles in D$_2$O was carried out

506   and the results compared with those for non-processed (EI)x2 under the same conditions.

507   Firstly, a solution of (EI)x2 in D$_2$O, at a concentration of 1 mg/ml and pH 7, was studied

508   by ^{1}H NMR spectroscopy at both 5 and 37°C (Figure 3A and B). The ^{1}H NMR spectrum

509   for (EI)x2 at 5°C (Figure 3A) shows the signals for protons at 0.6 ppm, corresponding to

510   the methyl groups of valine and isoleucine, 0.8 and 1.2 ppm (two signals integrating for

511   117 and 123 protons, respectively, and corresponding to the methylene group from

512   isoleucine), 1.5-2.0 ppm (signals corresponding to methylene groups from proline and the

513   methine groups from valine and isoleucine) and 3.2-4.4 ppm (signals corresponding to

514   the methine and methylene groups from the main amino acid chain). The values for the

515   signals and integrals are in agreement with those predicted for (EI)x2, with the presence

516   of signals for the hydrophobic and hydrophilic blocks indicating a non-aggregated

517   conformation for the biopolymer (Figure 3A).

518
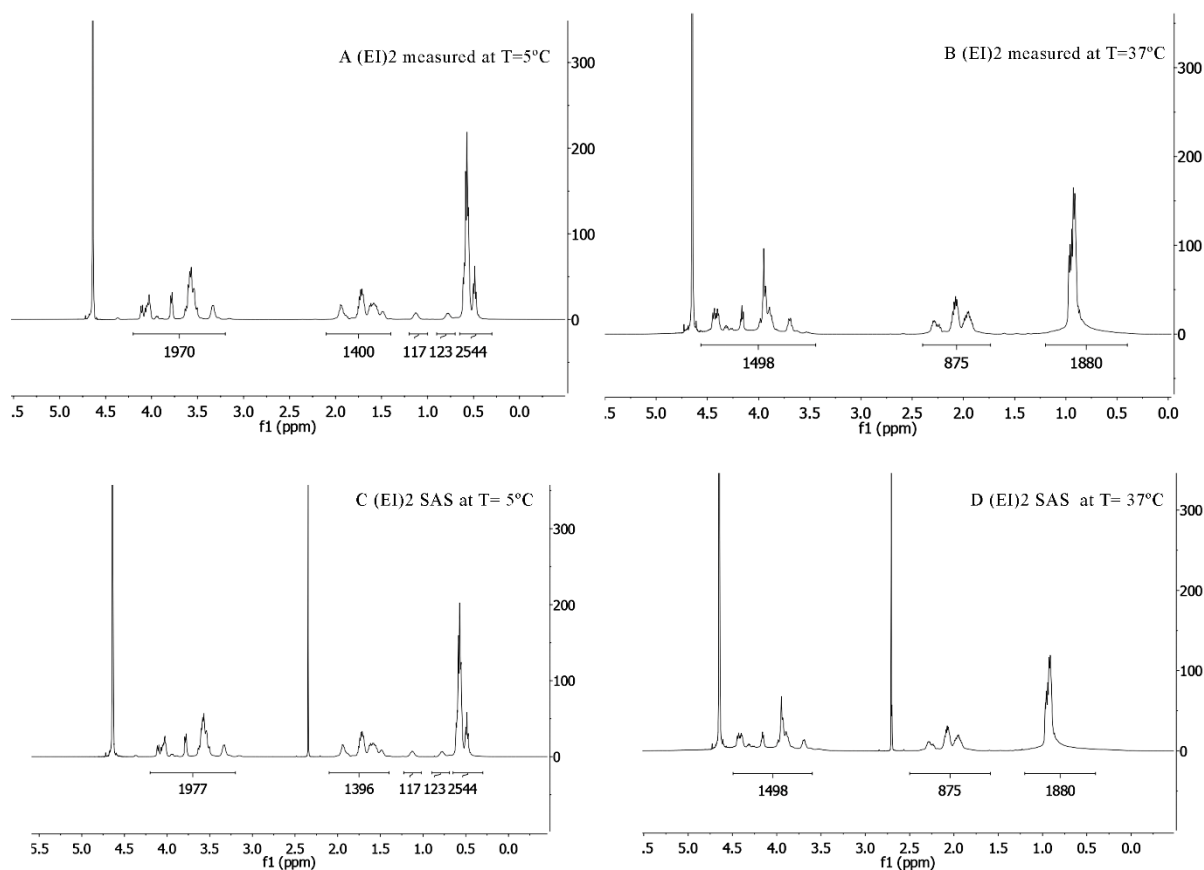
Figure 3. ^{1}H NMR spectrum of pure (EI)x2 at 5 (A) and 37°C (B) and (EI)x2 after the SAS process from experiment 4 (Table 1) at 5 (C) and 37°C (D).

However, the spectrum for (EI)x2 at 37°C (Figure 3B) shows the absence of the signals at 0.8 and 1.2 ppm corresponding to the isoleucine residues from the hydrophobic block. Moreover, a general reduction in the other signals is observed, and the residual integrals are in agreement with those for the hydrophilic block, i.e., 1880 protons for the methyl groups of valine at 0.6 ppm, 875 protons for the methylene groups of proline and the methine groups of valine at 1.5-2.0 ppm, and 1498 protons for the main amino acid chain at 3.2-4.4 ppm. The lack of signals for the hydrophobic block is in agreement with the aggregation of the biopolymer into nanoparticles, in which the hydrophobic block at the core is not detectable using this technique and the hydrophilic block is exposed at the corona, at this temperature (above Tt). This finding agrees with that for the

533   ~~NP~~nanoparticles analy~~sz~~ed in the DLS assay for (EI)x2 and their negative ζ-potential

534   value (Table 2).

535

536   The same procedure was performed with the powder obtained after processing (EI)x2

537   using the SAS technique. The ^{1}H NMR spectrum was found to be identical to that for

538   (EI)x2 at the same temperatures (Figure 3C and D), except for the signal for residual

539   DMSO at 2.49 ppm. Indeed, the spectrum recorded at 37°C (Figure 3D) shows the signals

540   and integrals corresponding exclusively to the hydrophilic block, with no signals

541   corresponding to the apolar block, in accordance with the formation of nanoparticles with

542   a hydrophobic core.

543

544   The ^{1}H NMR spectrum of (EI)x2-SAS solution at 5°C (Figure 3C) shows identical signals

545   and integrals to those for (EI)x2 (Figure 3A) at the same temperature. The presence of

546   signals for both blocks again indicates a non-aggregated conformation for the biopolymer.

547

548   A comparison of the ^{1}H NMR spectra recorded under the same conditions show~~eds~~ a

549   similar behavior for (EI)x2-SAS microparticles and unprocessed (EI)x2 biopolymer in

550   aqueous solution (Figure S5), thus demonstrating that the SAS technique does not alter

551   the ELR transition and that the self-assembly of ELRs into stable nanoparticles can be

552   achieved with (EI)x2 microparticles processed using the SAS technique in a top-down

553   approach involving reorganization in aqueous solution at 37°C.

554

555   *3.2 Encapsulation of DTX by ELRs*

556   Experiments studying the encapsulation of DTX by the ELRs ((EI)x2 and (EI)x2RGD)

557   were carried out under previously established experimental conditions (30 mg/mL, 35°C,

558 ~~110 bar~~11 MPa, coaxial nozzle and drying method 3) with a biopolymer:drug ratio of 1:1

559 (w/w). Experiments with (EI)x2 and (EI)x2RGD were also carried out in the absence of

560 DTX, using each as a control in subsequent cell assays.

561

562 The amount of residual DMSO in the microparticles was similar to that obtained for

563 experiment 4 (Table 1) under the operating conditions selected (3.4% and 3.1% for (EI)x2

564 and (EI)x2RGD lacking DTX, respectively). For the SAS experiments with DTX, the

565 initial 1:1 (w/w) ELR:DTX ratio used was not maintained in the resulting microparticles,

566 which exhibited a final ratio of 1:1.5, with the presence of 57.9% and 57.8% DTX and

567 3.5% and 3.7% residual DMSO for (EI)x2 and (EI)x2 RGD, respectively. This change in

568 the mass ratio is probably due to the ELR forming stronger hydrogen bonds with DMSO

569 and some ELR not precipitating, thus suggesting that a higher affinity for DMSO reduces

570 the antisolvent effect of the $scCO_2$. This new ratio was taken into consideration in

571 subsequent cell assays.

572

573 (EI)x2 DTX microparticles were also analyzed by SEM (Figure 4A), although no marked

574 difference in particle size compared~~with respect~~ to the experiments reported previously

575 was observed. It is striking that the small fibers seen in the SEM images (Figure 2) for

576 pure (EI)x2 are not present in Figure 4. This effect could be explained because~~is probably~~

577 ~~due to the fact that~~ the drug facilitates the nucleation of the polymer around it, thus

578 avoiding the formation of small fibers, by precipitating first.

579

580 *3.2.1. Behavior in aqueous solution*

581 Particle sizes were measured by DLS using aqueous solutions of the DTX-containing

582 particles at neutral pH, 37°C and a concentration of 1 mg/mL. The stability was followed

583   over a period of 5 days. Table 3 shows the values for D(0.5), PDI and ζ-potential and, as

584   expected, the ELR controls have similar values to those found in Table 2, with a D(0.5)

585   of around 40 nm, PDIs of less than 0.2 and a ζ-potential of around -30 mV. During the

586   stability assay, (EI)x2+DTX and (EI)x2RGD+DTX maintain similar values within a

587   small range of variation (Table 3) thus clearly indicating that these systems are stable

588   over time.

589

Sample	Day 0			Day 3			Day 5		
	D(0.5) (nm)	PDI	ζ-Potential (mV)	D(0.5) (nm)	PDI	ζ-Potential (mV)	D(0.5) (nm)	PDI	ζ-Potential (mV)
(EI)x2	43 ± 10	0.170 ± 0.002	-28.8 ± 3.1	32 ± 11	0.185 ± 0.008	-32.3 ± 3.2	38 ± 15	0.063 ± 0.005	-29.8 ± 4.2
(EI)x2RGD	36 ± 12	0.184 ± 0.007	-29.5 ± 2.5	40 ± 15	0.072 ± 0.006	-30.5 ± 2.6	37 ± 10	0.092 ± 0.003	-31.6 ± 1.3
(EI)x2 + DTX	45 ± 14	0.194 ± 0.006	-31.1 ± 2.2	42 ± 15	0.069 ± 0.003	-28.4 ± 1.8	35 ± 11	0.165 ± 0.004	-30.3 ± 20.1
(EI)x2RGD + DTX	40 ± 12	0.174 ± 0.005	-30.4 ± 4.1	37 ± 16	0.128 ± 0.007	-34.6 ± 2.2	41 ± 16	0.136 ± 0.004	-33.7 ± 4.1

590
591   **Table 3.** Values for the diameter, PDI and ζ-potential at different times during the stability

592   assay (37°C and neutral pH).

593

594   Transmission electron microscopy (TEM) was used to confirm the results obtained by

595   DLS. Figure 4B shows nanoparticles with an average size of 27.9 ± 4.4 nm, similar to

596   those reported in Table 3, which form due to the amphiphilic nature and self-assembly

597   behavior of the biopolymer. It can be also seen that there is no tendency to form large

598   agglomerations, in accordance with the PDI values obtained from the DLS results.
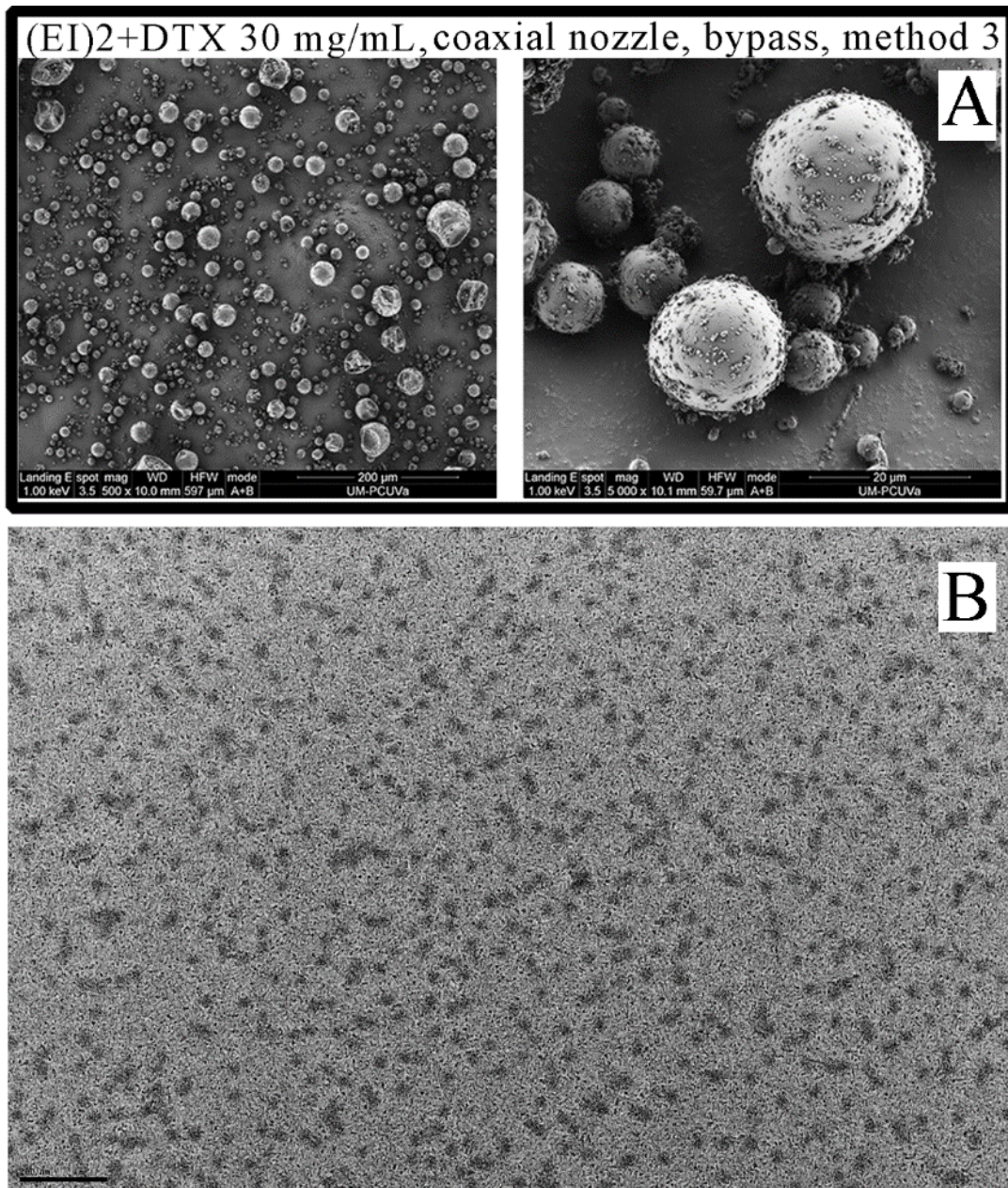
Figure 4. A) SEM Photomicrographs showing general (scale bar: 200 µm; magnification: x500) and detailed views (scale bar: 20 µm; magnification: x5000) of (EI)x2+DTX microparticles. B) TEM photomicrograph of (EI)x2+DTX prepared at a concentration of 1 mg/mL in ultrapure deionized water, at neutral pH and room temperature, with negative staining (scale bar: 200 nm).

~~In addition~~Also, it should be noted that the stability test was carried out with a DTX concentration of 0.6 mg/mL resulting from the starting SAS-microparticle solution (concentration of 1 mg/mL concentration), which implies that, as a result of the ELRs

609   used to co-precipitate DTX in the SAS process, it is possible to increase the solubility of

610   DTX in an aqueous medium by approximately fifty orders of magnitude. This result

611   would allow the use of solvents such as polysorbate 80 and ethanol in conventional

612   treatments with this drug to be avoided [48].

613

614   The encapsulation of DTX into the nanoparticles was studied by ^{1}H NMR spectroscopy

615   by recording the spectrum of an aqueous solution of (EI)x2+DTX microparticles from the

616   SAS process in D_2O (1 mg/ml, pH 7 and 37°C) as in the DLS assay (Table 3).

617

618   The spectrum obtained at 37°C (Figure 5A) is similar to that obtained for (EI)x2

619   microparticles (Figure 3A and C) and shows the same signals and integrals for the

620   hydrophilic glutamic acid block. The only difference compared~~with respect~~ to the

621   previous spectra is the appearance of very small and broad signals in the range 6.7-7.7

622   ppm and at around 1 ppm that could correspond to DTX molecules present in small

623   quantities on the surface of the core, which are responsible for the burst effect when

624   released, as shown in section 3.3. As such, this result is in accordance with the formation

625   of nanoparticles with a hydrophobic core and results from~~is in agreement with those found~~

626   ~~by~~ DLS or TEM (Table 4 and Figure 4B). Thus, the almost complete absence of DTX

627   signals could allow us to conclude that a correct encapsulation of DTX drug has been

628   achieved.

629

630   When the sample was cooled to 5°C (Figure 5B), the spectrum showed the signals from

631   the (EI)x2 biopolymer in a non-aggregated conformation, as can be deduced from the

632   signals for the methyl groups of valine and isoleucine at 0.6 ppm and the signals for the

633   methylene groups of isoleucine at 1.2 ppm. The presence of signals in the range 6.7-7.7

634   ppm due to the protons of DTX should also be noted. This result shows that DTX was

635   delivered from the core of the nanoparticles and confirms that the drug was encapsulated

636   inside those nanoparticles.

637

638   When this sample was again heated to 37°C, the NMR spectrum obtained (Figure S6)

639   was found to be identical to that shown in Figure 5A. The spectrum shows a similar

640   absence of DTX signals to that found after nanoparticle formation, thus meaning that

641   DTX is embedded in the hydrophobic core. Consequently, we can conclude that DTX is

642   trapped inside the ELR particles during the SAS process and that the solubility thereof is

643   improved, probably due to a non-covalent interaction with the ELR. In this respect, the

644   ability of the SAS technique to bring the ELR closer to the hydrophobic drug allows ~~an~~

645   interaction between them and also contributes to subsequent encapsulation.

646
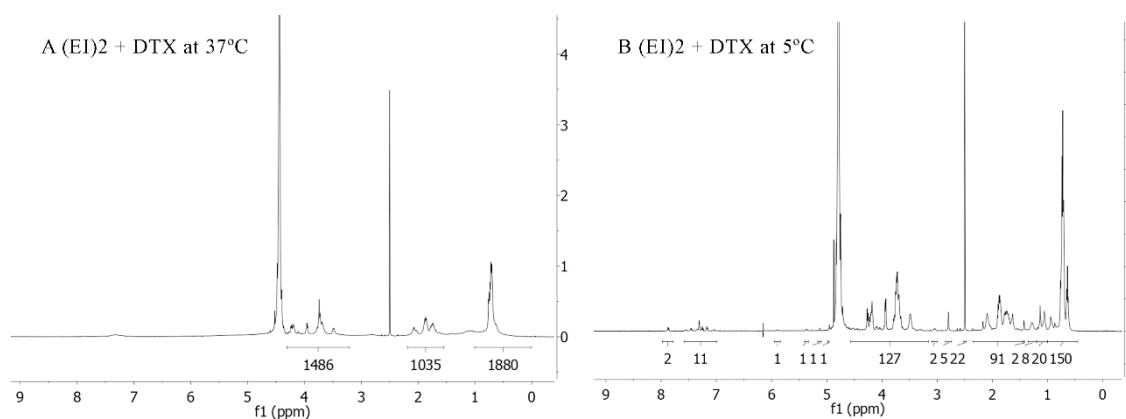
648   **Figure 5.** ^{1}H NMR spectrum of (EI)x2+DTX encapsulated at 37 (A) and 5°C (B).

649

650   As a control, a mixture of unprocessed (EI)x2 polymer and DTX, at the same weight ratio

651   as in the previous assays, was prepared and the NMR spectrum was acquired (Figure

652   S7A). The spectrum recorded at 37°C showed identical signals and integrals to those

653   shown above for (EI)x2 (Figure 3C) or ~~for~~ (EI)x2+DTX (Figure 5A) using the SAS

654   technique, in accordance with the formation of nanoparticles with a hydrophobic core.

655 Upon cooling the sample to 5°C, the NMR spectrum showed the presence of non-

656 aggregated (EI)x2 biopolymer, with the presence of DTX being practically negligible

657 (Figure S7B). This finding is in accordance with the absence of DTX inside the

658 hydrophobic core of the nanoparticle at 37°C, thereby confirming the need for SAS-type

659 processing to enable this hydrophobic drug (DTX) to be embedded into the core of the

660 (EI)x2 nanoparticle.

661

662 *3.3 Drug-release study*

663 A kinetic release study was performed by comparing (EI)x2+DTX with pure DTX ~~in~~

664 ~~order~~ to determine the quantity of drug delivered at each time point. Figure 4 shows the

665 percentage of drug released from the (EI)x2+DTX particles and percentage of drug

666 released from the control samples, in both cases for an experimental time of 96 hours.

667 Each point represents the result of an analysis in triplicate, with the standard deviation

668 represented in the error bars. As can be seen for the (EI)x2+DTX particles, $55 \pm 11\%$ of

669 the drug is released in the first 10 hours of the experiment, with the release velocity

670 subsequently decreasing until total release at 96 hours. However, in the control sample,

671 $53 \pm 2\%$ is released in the first 2 hours, with all the drug having been released after 24

672 hours. These results show a clear delay in the delivery of the drug from the co-precipitated

673 (EI)x2+DTX particles as it must cross the polymer barrier to reach the release medium,

674 which could prove useful for sustained release purposes.

675

676
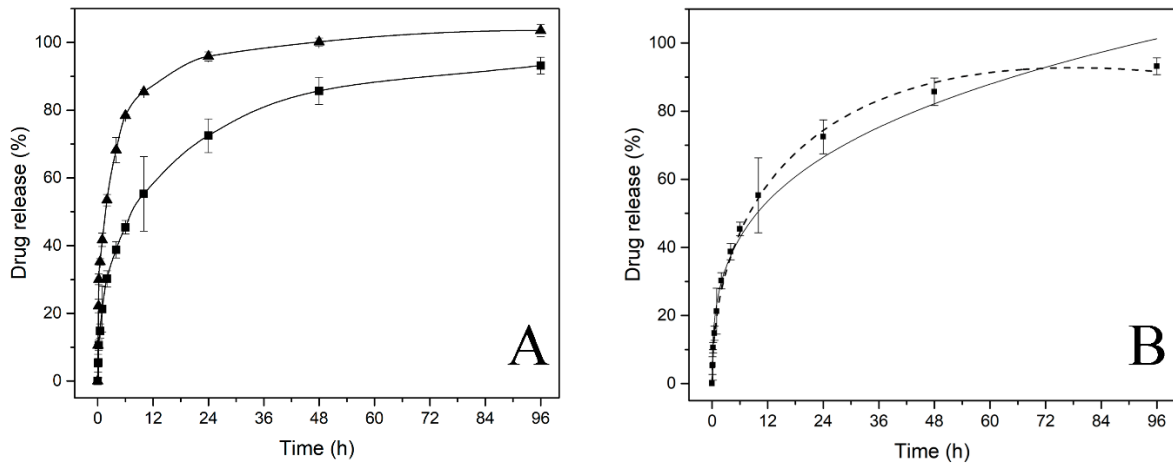
Figure 6. A) Study of drug release from (EI)x2+DTX and free DTX control sample vs. time (h) at a normalized DTX concentration of 0.6 mg/mL in water:ethanol (7:3) release medium. ■: (EI)x2 + DTX ▲: Free DTX control. Lines are used to guide the eye. B) Graphical fitting of the different mathematical models used to describe the release of DTX from (EI)x2 + DTX (■). Dashed line: Peppas–Sahlin fitting; solid line: Lindner–Lippold fitting.

~~In order to~~To understand the drug-delivery process, the experimental profile was mathematically fitted using the models described in section 2.2.3.2. To get a more accurate description of the process, three-time frames were defined (Table 4 and Figure 6B). Both models fit satisfactorily, ($R^2 > 0.980$), with the fit being slightly better for the Peppas–Sahlin equation. As can be seen from Table 4, the coefficient n from the Peppas–Sahlin equation has values of $0.5 < n < 1$ in the three-time periods, which suggests anomalous transport due to the slow rearrangement of polymeric chains and the diffusion process occurring simultaneously, thus resulting in time-dependent anomalous effects. However, between 0~~1~~ and 24 hours, n has a value of close to 0.5, thus indicating that release depends on diffusion of the fraction of docetaxel occluded in the material and close to its surface through the polymer matrix. Between 0~~24~~ and 96 hours, the diffusion

695 process becomes slower as DTX must diffuse through the nanoparticle to reach the release

696 medium.

697

698 Furthermore, the Peppas–Sahlin equation shows that the coefficient k_1 predominates in

699 all stages, thus meaning that the process is clearly governed by the Fickian diffusion

700 mechanism. These results are in agreement with those reported in the literature with the

701 same ELR in a hydrogel configuration [11, 19]. Likewise, the coefficient b (burst effect)

702 in the Lindner-Lippold equation is small and negative, thus indicating that the quantity of

703 DTX present on the surface of the particles is practically negligible, in agreement with

704 the conclusions for the solution behavior of SAS-processed (EI)x2+DTX particles from

705 the NMR spectroscopy study.

706

Model	Peppas–Sahlin				Lindner–Lippold			
Time frame (h)	k1	k2	n	COD R²	k1	n	b	COD R²
0 - 1	0.263 ± 0.030	-0.050 ± 0.031	0.615 ± 0.054	0.999	0.221 ± 0.005	0.529 ± 0.026	-0.001 ± 0.004	0.999
01 - 24	0.226 ± 0.003	-0.016 ± 0.001	0.503 ± 0.014	0.999	0.240 ± 0.020	0.367 ± 0.023	-0.022 ± 0.018	0.994
024 - 96	0.228 ± 0.05	-0.014 ± 0.001	0.464 ± 0.008	0.999	0.295 ± 0.047	0.281 ± 0.030	-0.055 ± 0.044	0.980

707
708 **Table 4.** Fitting of the profiles for release of DTX from (EI)x2+DTX processed using the

709 SAS technique to the Peppas–Sahlin and Lindner–Lippold equations using samples

710 prepared at a normalized concentration of 0.6 mg/mL during the different time frames.

711

712 *3.5 Effect of nanoparticles on cell viability*

713 Once the microparticles and their behavior in aqueous media had been completely

714 characterized, their effect on human cells was determined using two different human cell

715 lines, namely MDA-MB-231 breast cancer cells and human endothelial HUVEC cells.

716   These cell lines were chosen <mark>since</mark><s>due to the fact that</s> both are well-known for their high

717   expression of surface integrin receptors [54], which are implicated in a wide range of

718   cancers [43]. As the RGD peptide (Arg–Gly-Asp) binds preferentially to $\alpha_v\beta_3$ and $\alpha_v\beta_5$

719   integrin heterodimers, this tripeptide motif has been widely studied for cancer targeting

720   purposes and is an excellent model to test novel targeted carriers for drug delivery as it

721   allows nanocarriers to enter cancerous cells [44].

722

723   Three different concentrations of free DTX (0.1, 1 and 10 µM), and the same DTX

724   concentrations encapsulated in both types of ELR nanoparticles, depending on the

725   presence of the RGD sequence, were tested (Figures 7, S7 and S8). Empty ELR

726   nanoparticles were used as <mark>a</mark> control <mark><s>in order</s></mark> to determine both the effect of carriers on

727   cells and the internalization process. These DTX concentrations were selected <mark>based on</mark>

728   <mark><s>the basis of</s></mark> the solubility of the drug and the standard concentrations used in the literature,

729   thus allowing us to study the therapeutic window for the drug. For example, Saw *et al.*

730   have demonstrated that 1 µM DTX-loaded liposomes and micelles decrease the viability

731   of SCC-7 cells by 40% and 20%, respectively [55]. Furthermore, 1 µM DTX-loaded

732   albumin nanoparticles showed *in vitro* effects on murine melanoma B16F10 (20% cell

733   viability) and breast cancer MCF-7 cells (10% cell viability) [56]. Our smart nanocarriers

734   were therefore expected to behave as accurate drug-delivery devices by improving the

735   effectiveness of the chemotherapeutic drug DTX on cancer cells and decreasing undesired

736   effects in healthy cells.

737

738   The cytotoxic effect of control nanoparticles was determined initially (Figures 7, S7 and

739   S8). Although this type of nanoparticle does not carry any drug, internalization could still

740   affect cell viability. Incubation with empty control nanoparticles, either containing the

741 RGD sequence or not, did not significantly affect the viability of either cell line. Indeed,

742 our results showed no differences between three different concentrations, thereby

743 corroborating previous studies from this group in which ELR-based biopolymers with

744 and without the RGD peptide were characterized and showed no cytotoxicity [11, 57]. As

745 such, we can conclude that, under our experimental conditions, control nanocarriers did

746 not result in a decrease in the viability of either cancerous or non-cancerous cells.

747

748 As regards the effect of free DTX, incubation of the cells with the highest drug

749 concentration (10 µM) for 24 hours induced a markedly toxic effect, with cell viability

750 diminishing to 3-5%. In contrast, when the lowest concentration was used for the same

751 time, cell viability was only slightly affected (92-93% cell viability), whereas an

752 intermediate concentration (1 µM) decreased cell viability to 23-29%. Interestingly, there

753 were no noticeable differences between the two types of cells used at any concentration,

754 thus meaning that DTX acts on any cell undergoing division and has no selective effect

755 for cancer cells (Figure 7A-B). This result is in accordance with previous reports by Liu

756 *et al*. and Wang *et al*., who demonstrated that the viability of HUVEC cells was also

757 dramatically affected after treatment with DTX [58, 59].

758

759 Furthermore, different effects could be seen when DTX-loaded nanoparticles were used.

760 Thus, ELR nanoparticles lacking the RGD sequence failed to improve the action of free

761 DTX at any drug concentration, and the effect on both cancerous and non-cancerous cells

762 was reduced. This can be explained by the fact that the encapsulated DTX is less available

763 for cells and the drug needs more time to act. However, when MDA-MB-231 cells were

764 treated with DTX-loaded RGD-containing nanoparticles, the effect of DTX was

765 improved compared to the free drug and DTX-loaded non-RGD-containing nanoparticles

766   (Figure 7B). Indeed, the encapsulation of DTX within RGD-containing nanoparticles

767   significantly improved the effectiveness of the drug by decreasing cancer cell viability

768   (10% and 78% for 1 and 0.1 µM, respectively) when compared to free DTX (25% and

769   93% for 1 and 0.1 µM, respectively) and DTX-loaded non-RGD-containing nanoparticles

770   (42% and 96% for 1 and 0.1 µM, respectively). As can be seen in Figure 7C, both cell

771   lines showed different behaviors when treated with 1 µM free DTX or 1 µM encapsulated

772   DTX. Thus, when cells were treated with DTX-loaded nanoparticles lacking the RGD

773   peptide, cell viability was higher since the encapsulation of the chemotherapeutic agent

774   decreased drug availability for the cells. Interestingly, when cells were treated with RGD-

775   containing nanoparticles carrying the drug, cancer cells were more affected than cells

776   treated with free DTX. Moreover, this effect was not seen in HUVEC cells, which showed

777   increased cell viability levels compared to free DTX. This different behavior in HUVEC

778   and MDA-MB-231 cells can be explained by the fact that cancer cells have an enhanced

779   ability to internalize as a consequence of the specific cancer targeting system and their

780   higher metabolic rate. The enhanced internalization of MDA-MB-231 cells was

781   demonstrated when treated with nanoparticles lacking RGD, as this cell line was more

782   affected. AlsoIn addition, DTX-loaded nanoparticles containing the RGD sequence were

783   found to be more toxic in breast cancer cells compared to HUVEC, thereby highlighting

784   the specific effect of the targeting sequence due to the overexpression of integrins.

785
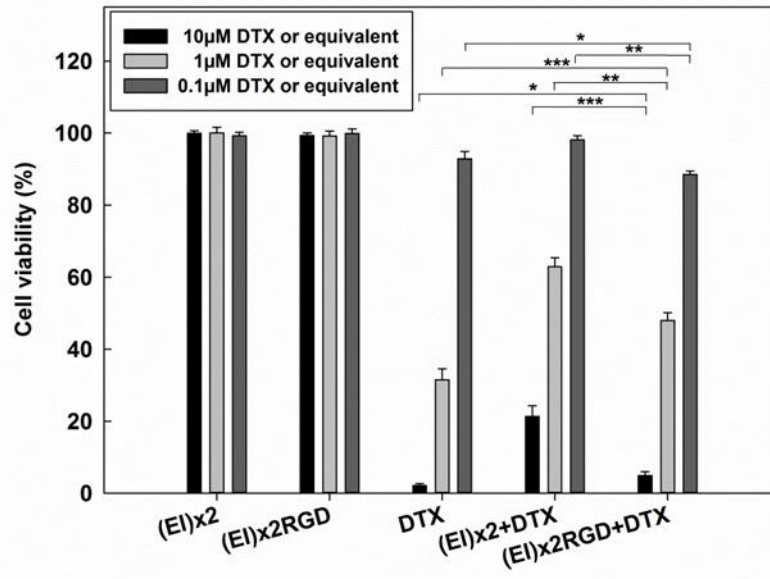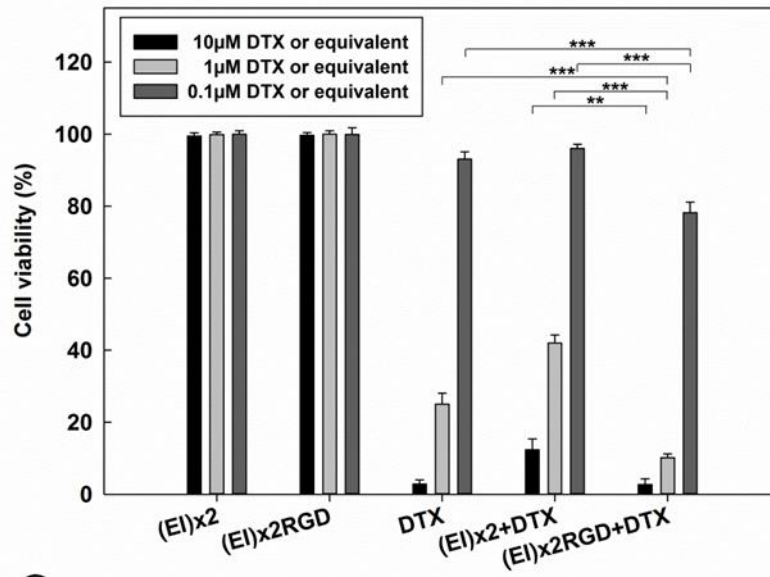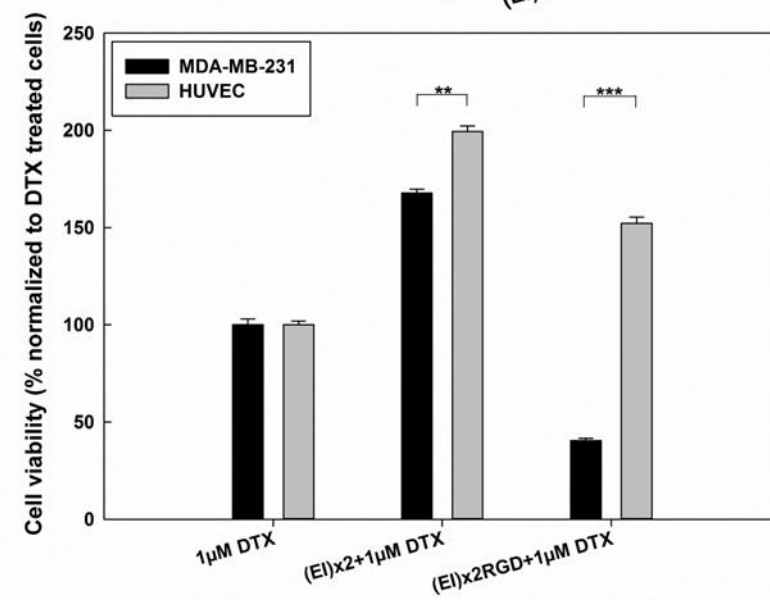
Figure 7. Percentage viability of HUVEC (panel A) and MDA-MB-231 cells (panel B). Cells were incubated with free DTX at three concentrations (0.1, 1 and 10 µM) or DTX encapsulated within ELR nanoparticles at the corresponding concentrations for 24 hours. Viability was measured using the LIVE/DEAD Assay kit. The percentage viability of both cell lines treated with 1 µM DTX-loaded ELR nanoparticles compared to free DTX treated cells (panel C). n = 3 independent experiments, mean ± SD. *p < 0.05, **p < 0.01, ***p < 0.001

3.6 Cell internalization of nanoparticles

The (EI)x2RGD nanoparticles were loaded with rhodamine using the SAS process and their cell internalization was corroborated by confocal microscopy. As can be seen in Figure 8, rhodamine-loaded nanoparticles were able to enter the cells and were localized in the perinuclear area in the cytoplasm. These images are in agreement with our hypothesis whereby the RGD cancer-targeting sequence facilitates the entry of ELR nanoparticles into the cells and release of the chemotherapeutic drug DTX into the cell cytoplasm, where the chemotherapeutic drug binds to the microtubules and blocks cell division.

805

806
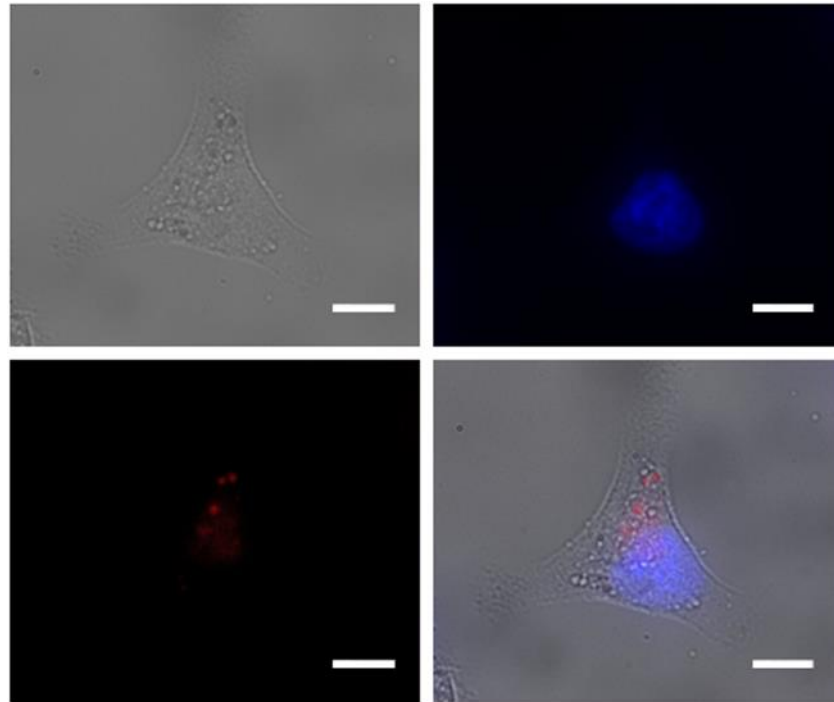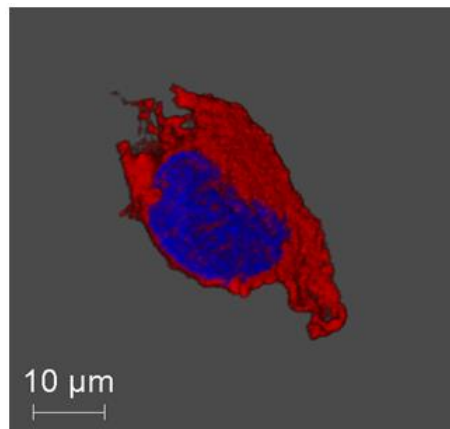
Figure 8. Fluorescence (Top panel) and confocal (Bottom panel) microscopy image of MDA-MB-231 cells treated with (EI)x2RGD nanoparticles with encapsulated rhodamine. Cell nuclei were stained with DAPI. Scale bars: 10 μm.

3.7 Effect of nanoparticles on cell proliferation

After determining their effect on cell viability, the ELR nanoparticles were then tested by measuring cell proliferation *in vitro* for 72 hours using MDA-MB-231 breast cancer cells incubated with 1 μM free or DTX encapsulated within ELR biopolymers by SAS. Thus, cell proliferation was determined every 4 hours by performing a cell confluence analysis [6], which allowed us to determine a real-time trend, rather than classical studies every

817   24 hours, which are unable to determine the accurate time of a change. This concentration

818   was chosen in light of the results shown in Figure 7, where it can be seen that 1 µM DTX

819   encapsulated within RGD-containing nanoparticles was more effective than free DTX in

820   breast cancer cells after treatment for 24 hours, although not in HUVEC cells. As such,

821   cell-proliferation assays were carried out over 72 hours ~~in order~~ to determine the effect

822   of DTX-loaded nanoparticles during several cell divisions.

823
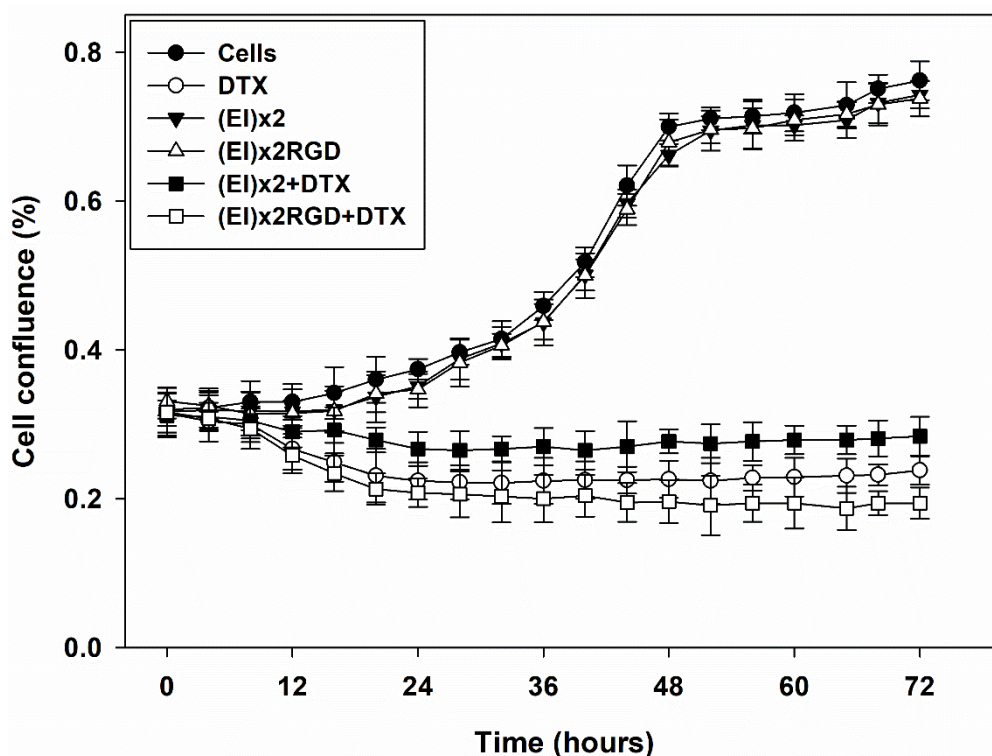
824
825   **Figure 9.** Cell proliferation of MDA-MB-231 analyzed by cell confluence measurements.

826   Cells were incubated with 1 µM free DTX, empty ELR nanoparticles or 1 µM DTX-

827   loaded ELR nanoparticles for 72 hours and confluence was measured using OMNI

828   software. Values are given as mean ± SD.

829

830   As shown in Figure 9, empty ELR nanoparticles, either with or without the RGD cell-

831   targeting sequence, ~~had no effect on~~ did not affect cell proliferation, with both types of

832   empty ELR nanoparticles exhibiting similar values to those for untreated cells.

833   Concerning~~With regard to~~ the trend in cell proliferation, breast cancer cells appeared to

834 start growing in an exponential mode after 12 hours, with cell proliferation ceasing after

835 48 hours and remaining stable up to 72 hours. This final stabilized period with no

836 proliferation could be due to a limitation of the nutrients available in the culture medium

837 after 3 days of highly proliferative growth.

838

839 However, when cancer cells were treated with 1 µM free DTX, cell proliferation stopped

840 after 12 hours of treatment and remained so up to 72 hours. As explained above (Figure

841 7), when MDA-MB-231 cancer cells were treated with 1 µM free DTX, the cell viability

842 after 24 hours was only 25%. As cell proliferation was not enhanced at any time point,

843 this could be explained because~~due to the fact that~~ the cancer cells were dead and ~~that~~ the

844 very small percentage of living cells present were unable to proliferate. Interestingly, the

845 same effect on proliferation was observed when cancer cells were treated with 1 µM DTX

846 encapsulated within nanoparticles lacking the RGD sequence. It should be noted that

847 these nanoparticles both improved the effect of DTX and that cell proliferation was higher

848 when compared with cells treated with free DTX. This result corroborated the finding

849 whereby encapsulation of the drug in ELR nanoparticles lacking the RGD sequence

850 diminishes the effect of the chemotherapeutic agent on cells, as was also seen in terms of

851 cell viability (Figure 7). Furthermore, when breast cancer cells were treated with 1 µM

852 DTX encapsulated within nanoparticles containing the RGD sequence, cell proliferation

853 was completely halted and exhibited even lower values compared to cells treated with

854 free DTX. This result is in agreement with Figure 7, which shows that DTX-loaded

855 nanoparticles containing the RGD sequence enhance the effect of free DTX on cells.

856 Thus, we can conclude that DTX provokes cell death and that surviving cells are unable

857 to proliferate, probably as a result of entering into a senescent state.

858

4. CONCLUSIONS

The operating conditions for producing docetaxel-loaded ELR microparticles using a supercritical antisolvent process have been established. This is a one-step process that avoids post-processing steps. The coaxial nozzle designed to improve the jet-spray inside the reactor managed to reduce the amount of residual solvent from 16% to 2.4% while still achieving high SAS process yields. As a result of the amphiphilic nature of the biopolymer, the drug-delivery device remained stable over time and showed a controlled DTX release profile following Fick-type diffusion processes. According to the stability tests, we have been able to increase the solubility of this highly hydrophobic anti-tumoral agent in aqueous solution by fifty orders of magnitude, thereby avoiding the use of surfactants.

After characterization of the ELR-based nanoparticles, their effect was measured *in vitro* in endothelial and breast cancer cells. The results showed that encapsulation of the chemotherapeutic drug in ELR nanoparticles lacking the RGD cancer-targeting sequence diminished the cell toxicity of DTX and, also, that breast cancer cells treated with DTX-loaded nanoparticles carrying the RGD sequence were more affected and showed lower cell viability than cells treated with free DTX. In contrast, this effect was not seen in HUVEC endothelial cells. As such, we have developed a novel drug-delivery system that is more accurate than the non-selective chemotherapeutic drug DTX alone and shows an enhanced effect in breast cancer cells compared to healthy endothelial cells, which would come into contact with such nanoparticles after systemic administration. Consequently, this smart ELR polymer could be a useful approach for drug-delivery purposes due to its ability to encapsulate highly hydrophobic drugs and incorporate different bioactive

883 peptides or sequences as targeting systems ~~in order~~ to achieve a more advanced tool for

884 cancer treatment than current non-specific chemotherapeutic agents.

885

886 **Conflict of interest**

887 The authors declare no competing financial interest.

888

889 **Acknowledgements**

899

900 **5. REFERENCES**

901 [1] R. Langer, Science. 249 (1990) 1527-1533. https://doi.org/10.1126/science.2218494
902 [2] M. Santos, S. Serrano-Ducar, J. Gonzalez-Valdivieso, *et al.*, Curr. Med. Chem. 26
903 (2018) 7117-7146. http://dx.doi.org/10.2174/0929867325666180508094637
904 [3] J.C. Rodríguez-Cabello, L. Martín, A. Girotti, *et al.*, Nanomedicine. 6 (2011) 111-
905 122. https://doi.org/10.2217/nnm.10.141
906 [4] J.C. Rodríguez-Cabello, I. González de Torre, A. Ibañez-Fonseca, *et al.*, Adv. Drug
907 Deliv. Rev. 129 (2018) 118-133. https://doi.org/10.1016/j.addr.2018.03.003
908 [5] M.J. Pina, A. Girotti, S. Serrano, *et al.*, Cancer Lett. 470 (2019) 43-53.
909 https://doi.org/10.1016/j.canlet.2019.11.031
910 [6] J. Gonzalez-Valdivieso, A. Girotti, R. Muñoz, *et al.*, Biomacromolecules. 20 (2019)
911 1996-2007. https://doi.org/10.1021/acs.biomac.9b00206
912 [7] J.C. Rodríguez-Cabello, A. Girotti, A. Ribeiro, *et al.*, in: Navarro M, Planell JA,
913 editors, Nanotechnology in Regenerative Medicine: Methods and Protocols, Humana
914 Press, Totowa, Yea, pp. 17-38.

915   [8] D.W. Urry, Prog. Biophys. Mol. Biol. 57 (1992) 23-57. https://doi.org/10.1016/0079-
916   6107(92)90003-o

917   [9] P.L. San Biagio, F. Madonia, T.L. Trapane, *et al.*, Chem. Phys. Lett. 145 (1988) 571-
918   574. https://doi.org/10.1016/0009-2614(88)87422-0

919   [10] G. Pinedo-Martín, M. Santos, A. Testera, *et al.*, Polymer. 55 (2014) 5314-5321.
920   https://doi.org/10.1016/j.polymer.2014.08.053

921   [11] A. Fernandez-Colino, J.M. Bermudez, F.J. Arias, *et al.*, Mater. Sci. Eng. C 61 (2016)
922   286-292. https://doi.org/10.1016/j.msec.2015.12.050

923   [12] J.S. Ryu, D. Raucher, Cancer Lett. 348 (2014) 177-184.
924   https://doi.org/10.1016/j.canlet.2014.03.021

925   [13] W. Wang, J. Despanie, P. Shi, *et al.*, J. Mater. Chem. B. 2 (2014) 8131-8141.
926   https://doi.org/10.1039/C4TB00979G

927   [14] J. Hu, L. Xie, W. Zhao, *et al.*, Chem. Commun. 51 (2015) 11405-11408.
928   https://doi.org/10.1039/C5CC04035C

929   [15] J.F. Nawroth, J.R. McDaniel, A. Chilkoti, *et al.*, Macromol. Biosci. 16 (2016) 322-
930   333. https://doi.org/10.1002/mabi.201500376

931   [16] L. Yildirimer, N.T.K. Thanh, M. Loizidou, *et al.*, Nano Today. 6 (2011) 585-607.
932   https://doi.org/10.1016/j.nantod.2011.10.001

933   [17] G. Ma, J. Control. Release. 193 (2014) 324-340.
934   https://doi.org/10.1016/j.jconrel.2014.09.003

935   [18] A. Elhenshir, A. Subkha, Energy Procedia. 37 (2013) 6964-6978.
936   https://doi.org/10.1016/j.egypro.2013.06.630

937   [19] A. Fernandez-Colino, D.A. Quinteros, D.A. Allemandi, *et al.*, Mol. Pharm. 14 (2017)
938   4498-4508. https://doi.org/10.1021/acs.molpharmaceut.7b00615

939   [20] E. Reverchon, Ind. Eng. Chem. Res. 41 (2002) 2405-2411.
940   https://doi.org/10.1021/ie010943k

941   [21] D.T. Santos, M.A. Meireles, J. Food Process Eng. 36 (2013) 36-49.
942   https://doi.org/10.1111/j.1745-4530.2011.00651.x

943   [22] R. Campardelli, L. Baldino, E. Reverchon, J. Supercrit. Fluid. 101 (2015) 193-214.
944   https://doi.org/10.1016/j.supflu.2015.01.030

945   [23] H. Zheng, J. Zhang, J. Yan, *et al.*, J. CO2 Util. 16 (2016) 272-281.
946   https://doi.org/10.1016/j.jcou.2016.08.002

947   [24] A. Martín, M.J. Cocero, Adv. Drug Deliv. Rev. 60 (2008) 339-350.
948   https://doi.org/10.1016/j.addr.2007.06.019

949   [25] M.J. Cocero, Á. Martín, F. Mattea, *et al.*, J. Supercrit. Fluid. 47 (2009) 546-555.
950   https://doi.org/10.1016/j.supflu.2008.08.015

951   [26] Á. Martín, K. Scholle, F. Mattea, *et al.*, Crystal Growth Des. 9 (2009) 2504-2511.
952   https://doi.org/10.1021/cg900003m

953   [27] D.T. Santos, A.L. Santana, M.A. Meireles, *et al.*, Supercritical Antisolvent
954   Precipitation Process: Fundamentals, Applications and Perspectives, SpringerBriefs in
955   Applied Sciences and Technology, Yea, pp. 75-82.

956   [28] P. Franco, I. De Marco, Processes. 8 (2020) 938-948.
957   https://doi.org/10.3390/pr8080938

958   [29] I.A. Uzun, O. Sipahigilb, S. Dinçer, J. Supercrit. Fluid. 55 (2011) 1059-1069.
959   https://doi.org/10.1016/j.supflu.2010.09.035

960   [30] A. Montes, M.D. Gordillo, C. Pereyra, *et al.*, J. Supercrit. Fluid. 94 (2014) 91-101.
961   https://doi.org/10.1016/j.supflu.2014.07.001

962   [31] V. Prosapio, E. Reverchon, I. De Marco, J. Supercrit. Fluid. 118 (2016) 19-26.
963   https://doi.org/10.1016/j.supflu.2016.07.023

964 [32] I. Palazzo, P. Trucillo, R. Campardelli, *et al.*, Food Bioprod. Process. 123 (2020)
965 312-321. https://doi.org/10.1016/j.fbp.2020.07.010
966 [33] N. Annabi, S.M. Mithieux, A.S. Weiss, *et al.*, Biomaterials. 30 (2009) 1-7.
967 10.1016/j.biomaterials.2008.09.031
968 [34] X. Huang, C. Yi, Y. Fan, *et al.*, Mater. Sci. Eng. C 42 (2014) 325-332.
969 https://doi.org/10.1016/j.msec.2014.05.041
970 [35] Y. Guo, W. He, S. Yang, *et al.*, Coll. Surf. B. 151 (2017) 119-127.
971 https://doi.org/10.1016/j.colsurfb.2016.12.012
972 [36] S. Jafari, M. Soleimani, R. Salehi, Int. J. Polym. Mater. 68 (2019) 859-869.
973 https://doi.org/10.1080/00914037.2018.1517348
974 [37] R.S. Jadon, M. Sharma, J. Drug Deliv. Sci. Tech. 51 (2019) 475-484.
975 https://doi.org/10.1016/j.jddst.2019.03.039
976 [38] http://www.hmdb.ca/metabolites/HMDB0015378 (Accessed January 2020).
977 [39] J. Cheng, B.A. Teply, I. Sherifi, *et al.*, Biomaterials. 28 (2007) 869-876.
978 https://doi.org/10.1016/j.biomaterials.2006.09.047
979 [40] L. Martin, F.J. Arias, M. Alonso, *et al.*, Soft. Matter. 6 (2010) 1121-1124.
980 https://doi.org/10.1039/B923684H
981 [41] Y. Hao, B. Zhang, C. Zheng, *et al.*, J. Control.Release. 220 (2015) 545-555.
982 https://doi.org/10.1016/j.jconrel.2015.11.016
983 [42] D.E. Meyer, A. Chilkoti, Nat. Biotechnol. 17 (1999) 1112-1115.
984 https://doi.org/10.1038/15100
985 [43] S.L. Goodman, H.J. Grote, C. Wilm, Biol. Open. 1 (2012) 329-340.
986 https://doi.org/10.1242/bio.2012364
987 [44] F.F. Lang, C. Conrad, C. Gomez-Manzano, *et al.*, J. Clin. Oncol. 36 (2018) 1419-
988 1427. https://doi.org/10.1200/jco.2017.75.8219
989 [45] D.W. Urry, Angewandte Chemie International Edition 32 (1993) 819-841.
990 [46] A. Natolino, C. Da Porto, S. Rodríguez-Rojo, *et al.*, J. Supercrit. Fluid. 118 (2016)
991 54-63. https://doi.org/10.1016/j.supflu.2016.07.015
992 [47] S. Akhtartavan, M. Karimi, K. Karimian, *et al.*, Biomed. Pharmacother. 109 (2019)
993 2427-2433. https://doi.org/10.1016/j.biopha.2018.11.110
994 [48] https://www.ema.europa.eu/en/documents/product-information/taxotere-epar-
995 product-information_es.pdf (Accessed April 2020).
996 [49] A.J. ten Tije, J. Verweij, W.J. Loos, *et al.*, Clin Pharmacokinet. 42 (2003) 665-685.
997 10.2165/00003088-200342070-00005
998 [50] https://www.ema.europa.eu/en/ich-q3c-r6-residual-solvents (Accessed May 2020).
999 [51] E. Haimer, M. Wendland, A. Potthast, *et al.*, J. Nanomater. 2008 (2008) 1-5.
1000 https://doi.org/10.1155/2008/826974
1001 [52] M. Kalani, R. Yunus, Int. J. Nanomed. 6 (2011) 1429-1442.
1002 https://doi.org/10.2147/IJN.S19021
1003 [53] J. Stetefeld, S.A. McKenna, T.R. Patel, Biophys. Rev. 8 (2016) 409-427.
1004 https://doi.org/10.1007/s12551-016-0218-6
1005 [54] T. Meyer, J.F. Marshall, I.R. Hart, Br. J. Cancer. 77 (1998) 530-536.
1006 https://doi.org/10.1038/bjc.1998.86
1007 [55] P.E. Saw, M. Yu, M. Choi, *et al.*, Biomaterials. 123 (2017) 118-126.
1008 https://doi.org/10.1016/j.biomaterials.2017.01.040
1009 [56] G. Battogtokh, O. Gotov, J.H. Kang, *et al.*, Nanomed. 13 (2018) 325-338.
1010 https://doi.org/10.2217/nnm-2017-0274
1011 [57] D. Pescador, A. Ibáñez-Fonseca, F. Sánchez-Guijo, *et al.*, J. Mater. Sci. 28 (2017)
1012 115-125. https://doi.org/10.1007/s10856-017-5928-1
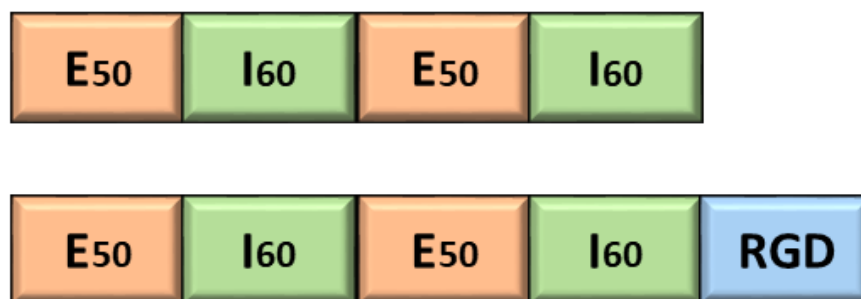
1013   [58] X. Wang, Y. Wang, X. Chen, *et al.*, J. Control. Release. 139 (2009) 56-62.
1014   https://doi.org/10.1016/j.jconrel.2009.05.030
1015   [59] F. Liu, M. Li, C. Liu, *et al.*, Pharm. Res. 31 (2014) 475-488.
1016   https://doi.org/10.1007/s11095-013-1176-3

1017

1018

Supporting Information

Non-coaxial nozzle: characteristics

The SAS pilot plant was originally equipped with a non-coaxial nozzle, which basically consist in a 1/16" pipe with 0.020" ID (Figure S1 B) for the solution inlet; the $scCO_2$ was pumped through an independent small opening of 1/4" situated in the top cover of the vessel next to the nozzle.

Coaxial nozzle: design characteristic

The new nozzle (Figure S2A and S2C) contains four grooves around a central cylinder that can be threaded into the top cover of the reactor, and a central hole through which a 1/16" stainless steel 0.020" ID pipe is inserted, which can be interchanged with another one of higher or lower ID. In this way, the $scCO_2$ at the desired flow produces the spray of the pumped solution, which always encounters fresh $scCO_2$ at the tip of the nozzle.

The non-coaxial nozzle is manufactured by fused deposition modelling (FDM) 3D printing since it allows pieces to be prototyped more cheaply and easily than other

techniques. Polyoxymethylene (POM) was chosen to manufacture the nozzle since this material allows a wide range of working temperatures (between -40 and 90 °C), has high mechanical strength, rigidity and hardness, as well as high shock resistance, excellent dimensional stability, and can be purchased cheaply.

A   B

C
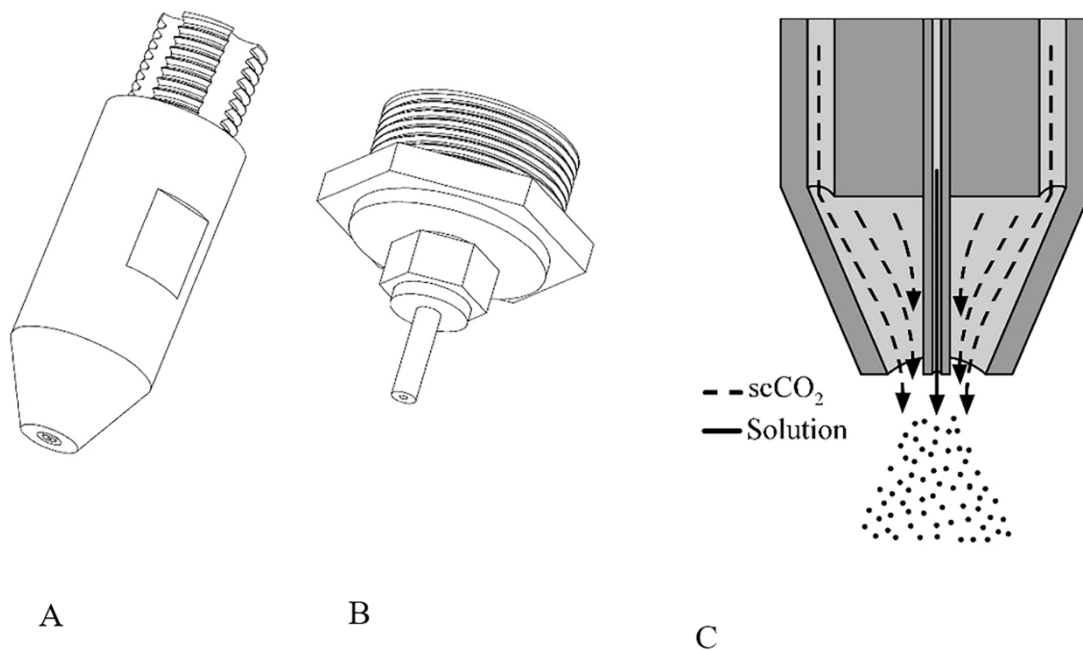
**Figure S21.** Representation of the nozzles used in the experiments. A: Coaxial nozzle; B: non-coaxial nozzle; C: representation of operation with the coaxial nozzle.

Determination of the Transition temperature (Tt)

In order to determine whether the use of $scCO_2$ changed the transition temperature (Tt) of the biopolymers, two samples, one of them with a high amount of residual DMSO from experiment 1 and the other one with low residual DMSO from experiment 4 was analysed by differential scanning calorimetry (DSC). Their behavior was compared with the (EI)2 without processing it, in order to determine whether the presence of residual DMSO affects their thermal behavior.

Sample	pH	ΔH (J·g^{-1})	T_t (ºC)
Exp. 1	7.22	-8.92	16.52
Exp. 4	6.92	-8.62	16.56
(EI)2	7.49	-8.76	16.50

Table S1. Transition temperatures and enthalpy for the processed ELR from experiments 1 and 4 and (EI)2 without SCF processing, as measured by DSC.
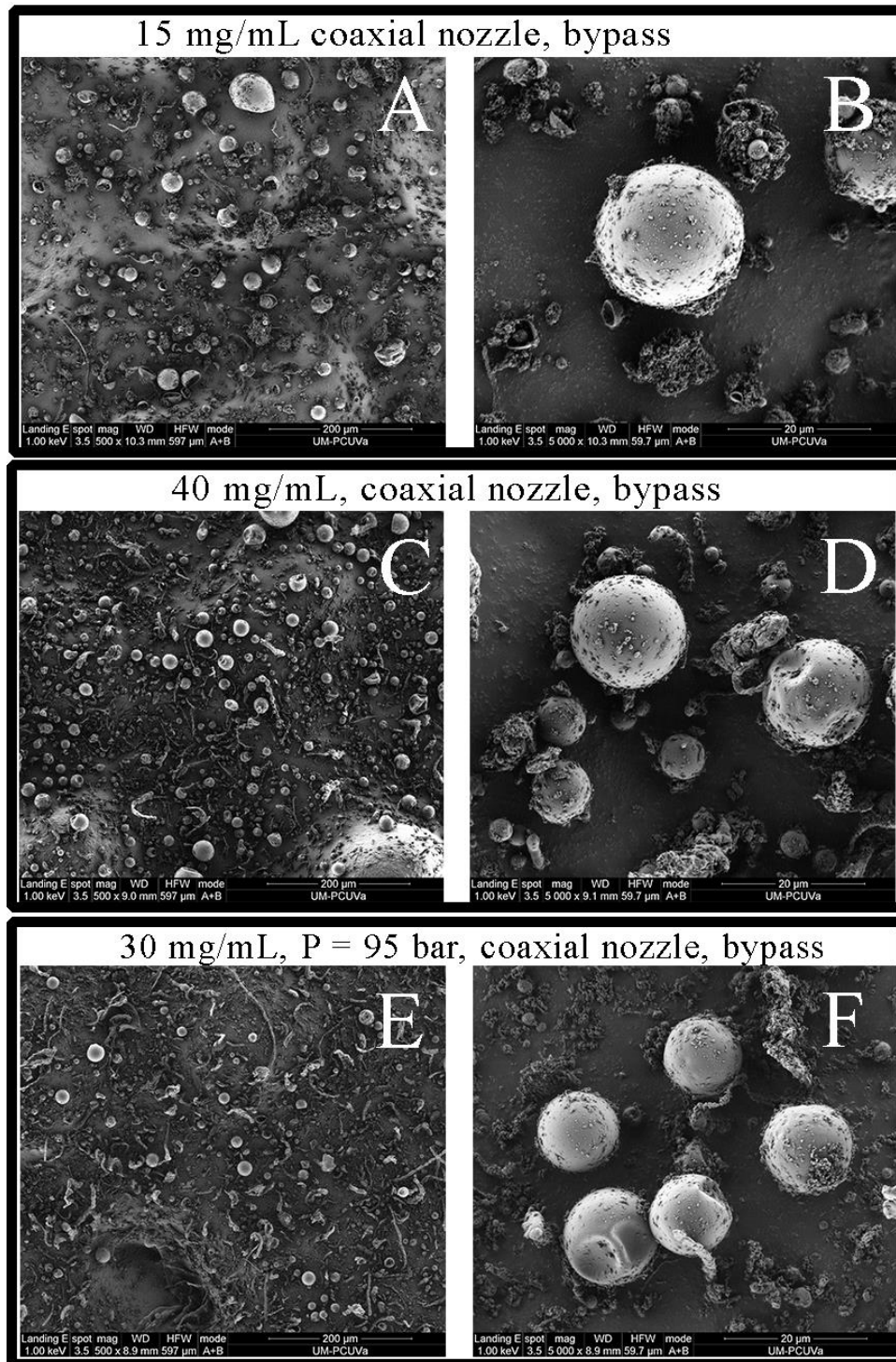
As can be seen from Table S1, there are no marked differences between the transition temperatures for the processed samples and the unprocessed ELR even when comparing experiments 1 and 4 (the product of experiment 1 contains around three times more residual DMSO than that from experiment 4). As such, it is clear that neither processing with scCO$_2$ or the quantity of residual DMSO found in the samples affects the thermal behavior of the ELRs.
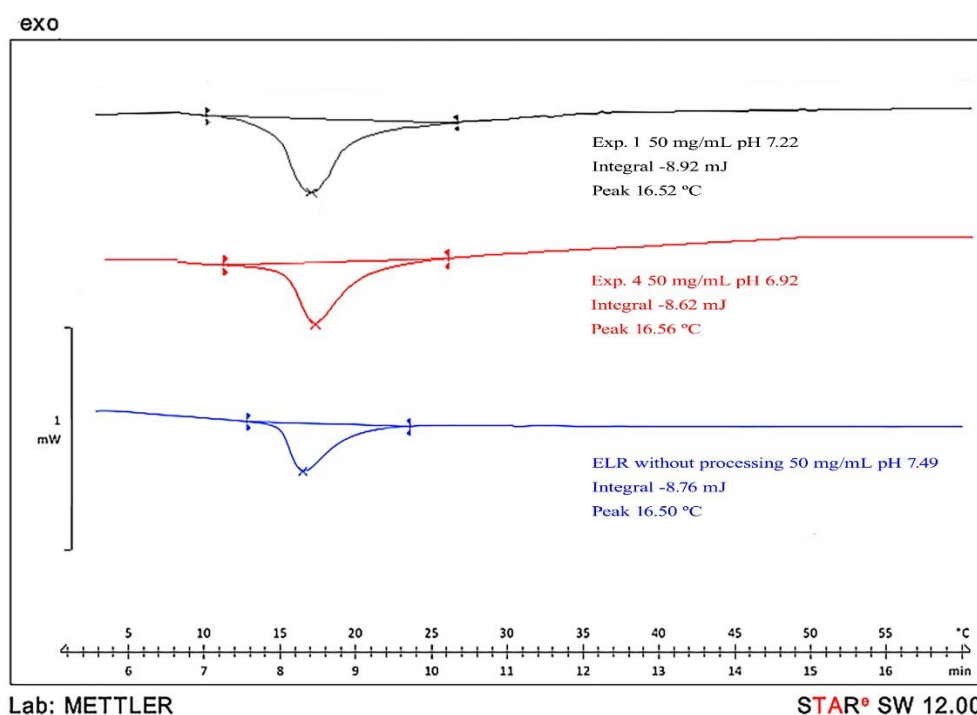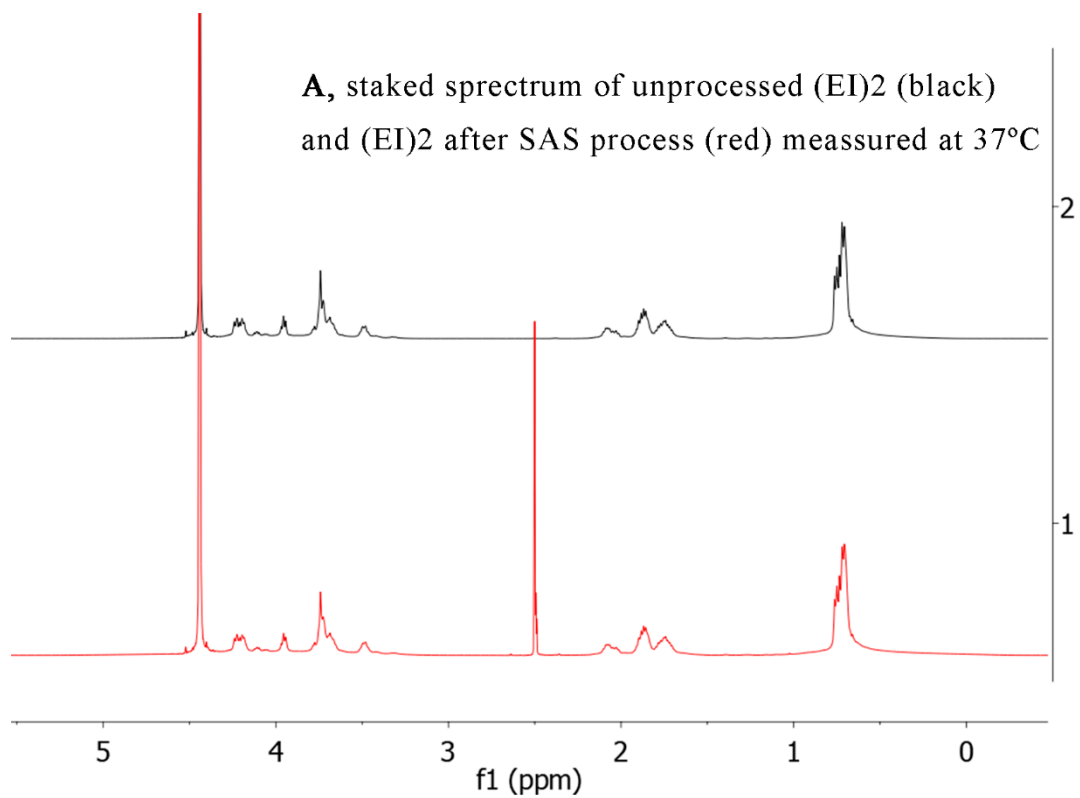
Figure S32. DSC thermograms for heating cycle (5°C/min from 0°C to 60°C) for unprocessed (green), (EI)2 from experiment 1 (black) and experiment 4 (red) at 50 mg/mL and pH 7.

SEM Photomicrographs

A, staked sprectrum of unprocessed (EI)2 (black) and (EI)2 after SAS process (red) meassured at 37°C

B, staked sprectrum of unprocessed (EI)2 (black) and (EI)2 after SAS process (red) meassured at 5°C
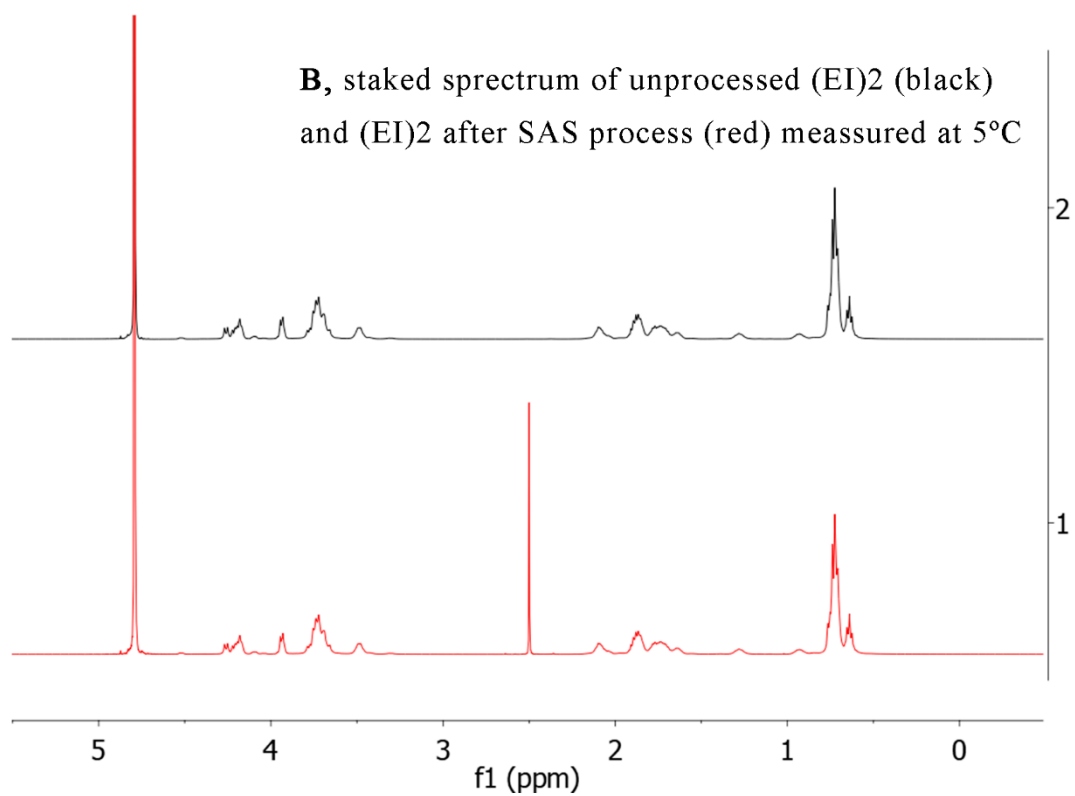
Figure S54. A: Staked spectrums of the (EI)2 (red) and (EI)2 after SAS process (black) at 37ºC. B: staked spectrums of the (EI)2 (red) and (EI)2 after SAS process (black) at 5ºC.

staked spectrums of the (EI)2 + DTX
at 37ºC (black) and (EI)2 + DTX
at 37ºC after cycle return(red)
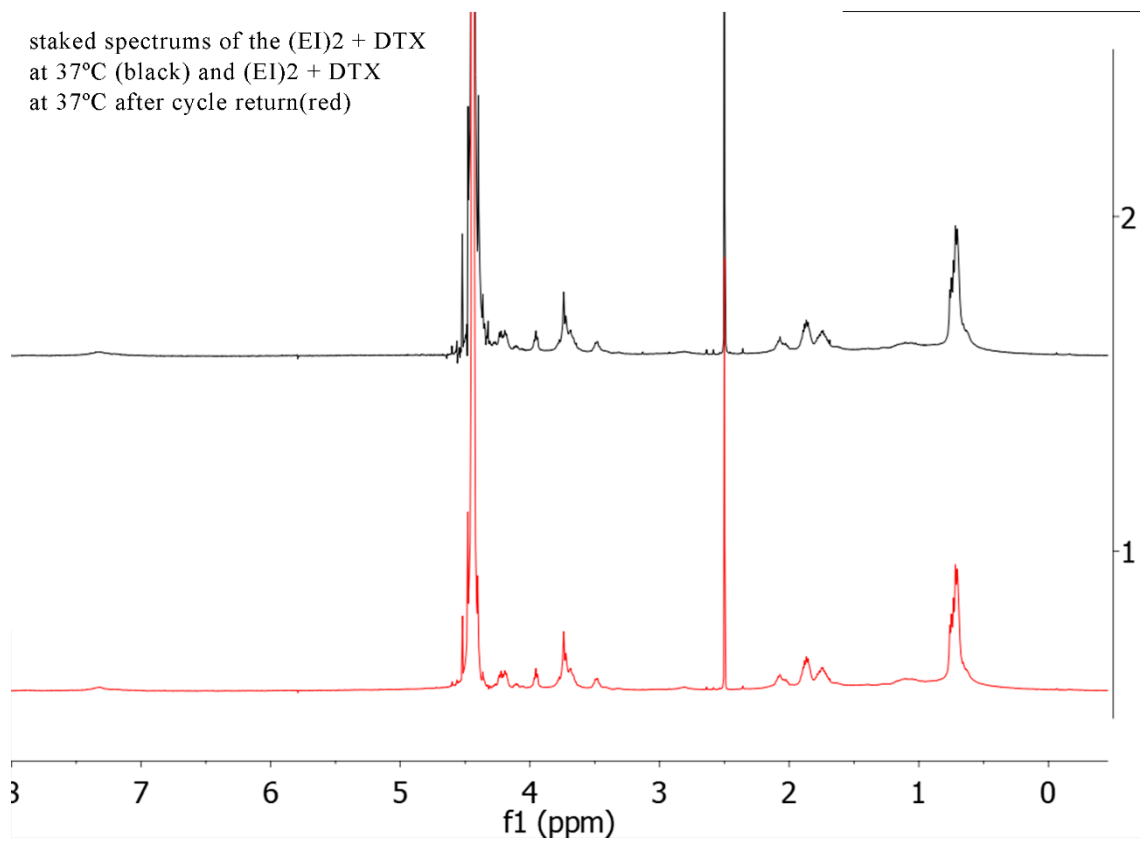
Figure S65. Staked spectrums of the (EI92+DTX at 37ºC (black) and (EI)2+DTX at 37ºC after cycle return (red).
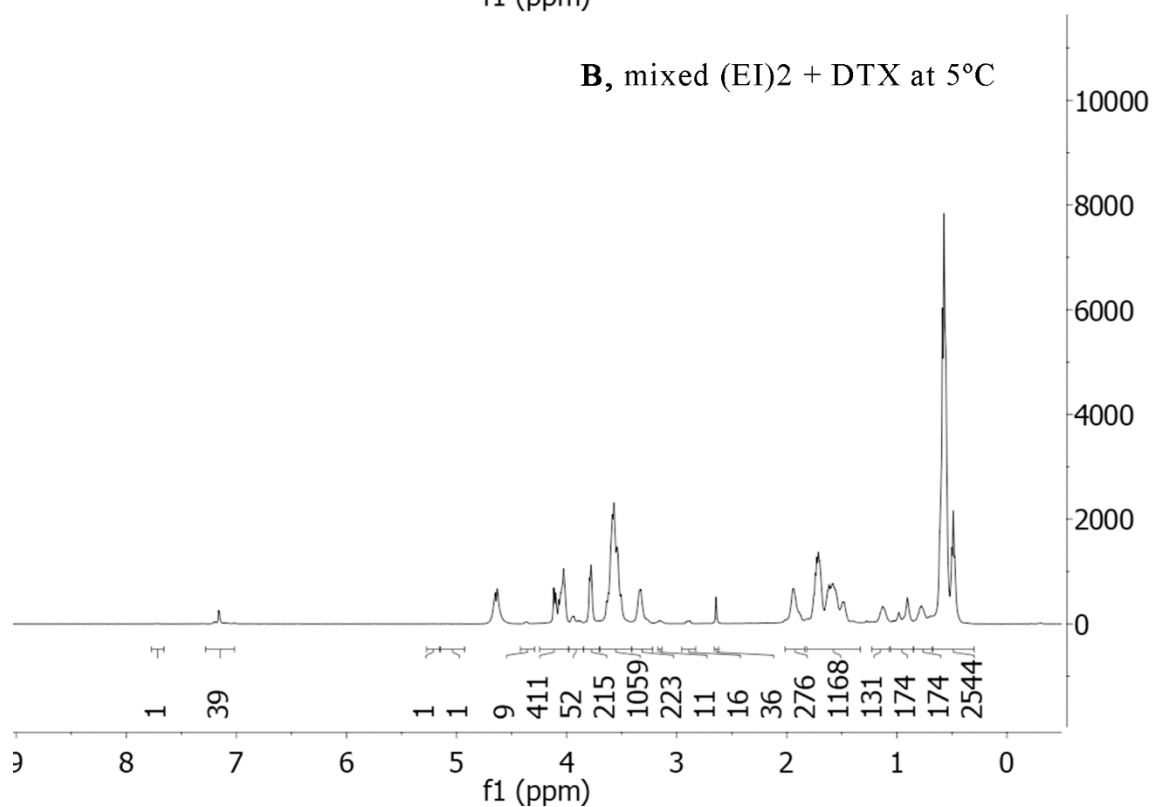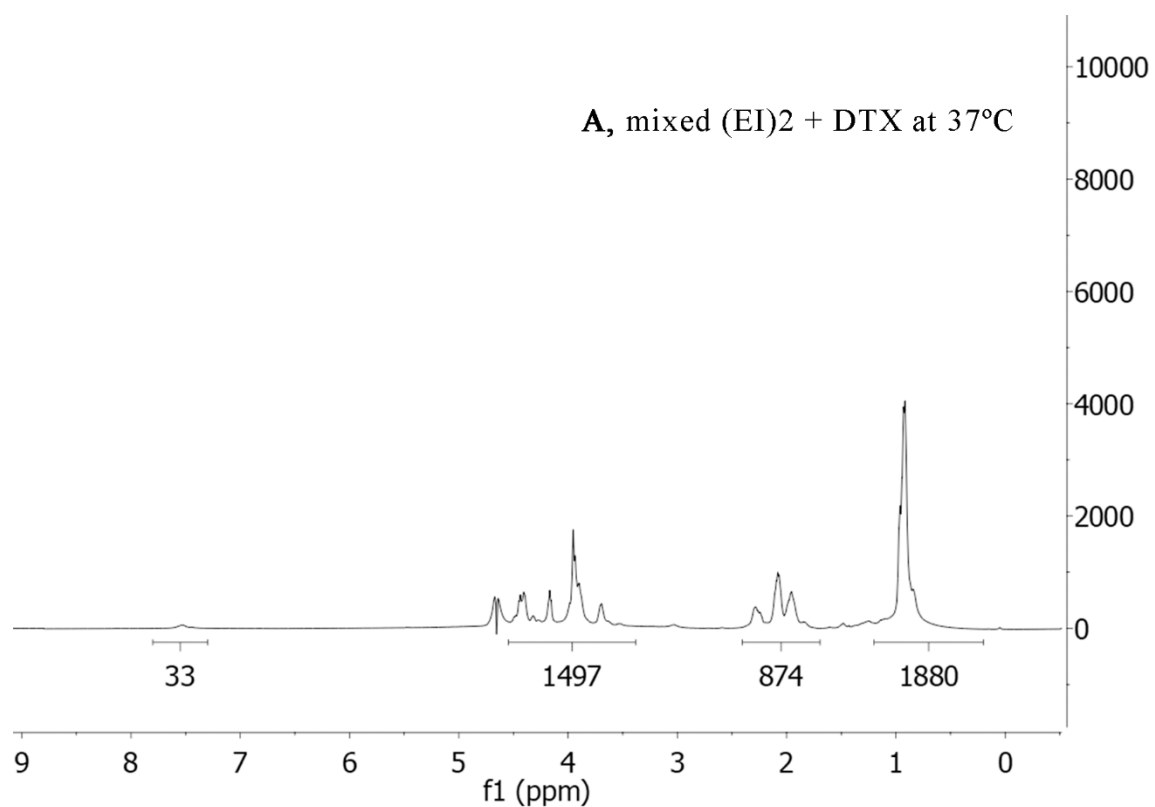
Figure S76. A: mixed (EI)2 + DTX at the same weight ratio at 37ºC. B: mixed (EI)2 + DTX at the same weight ratio at 5ºC.

Sample	DTX concentration (µM)	Corresponding ELR concentration (mg/L)
(EI)2+DTX	0.1	0.0543
	1	0.543
	10	5.43
(EI)2RGD+DTX	0.1	0.0543
	1	0.543
	10	5.43

Table S2. Encapsulated DTX concentrations and the corresponding ELR concentrations.
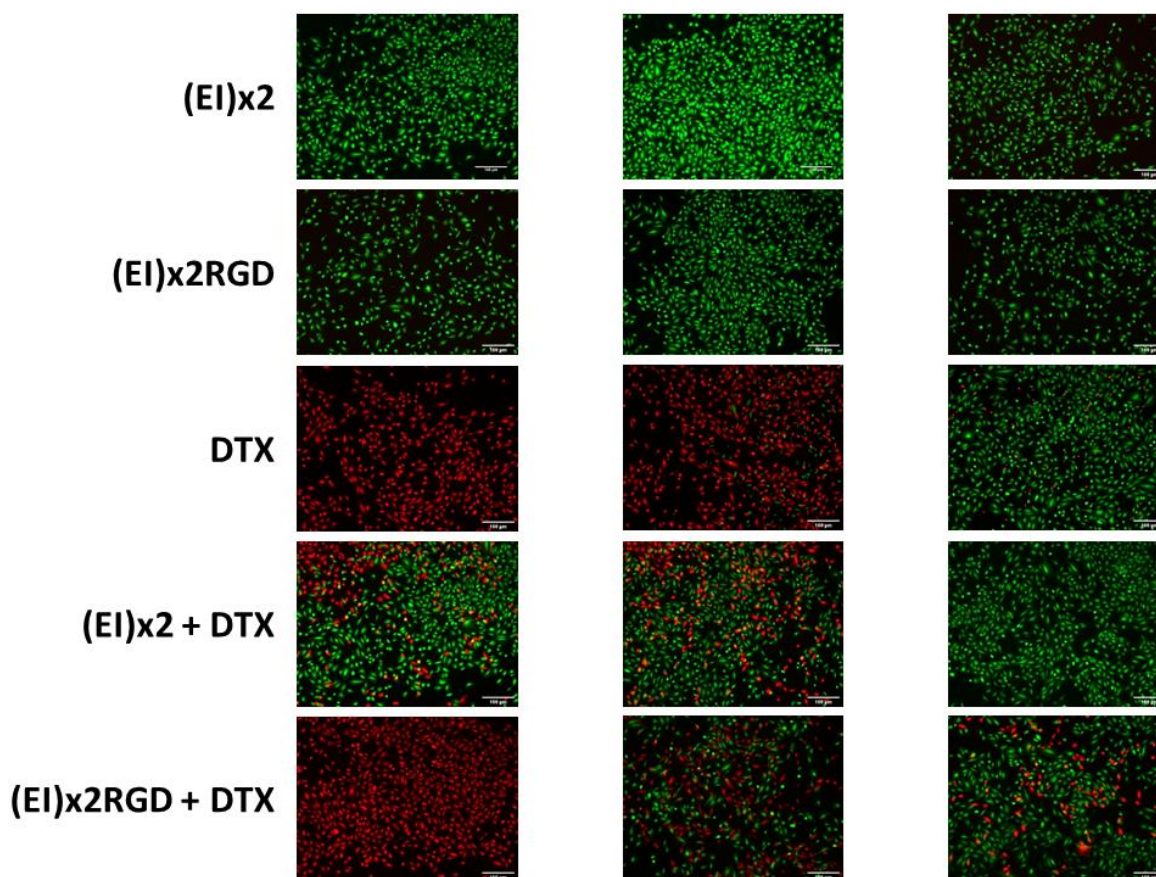
Figure S87. Representative fluorescence microscopy images for HUVEC cells after incubation with free DTX at three concentrations [0.1 (right column), 1 (middle column) and 10 µM (left column)] or encapsulated DTX within ELR nanoparticles at the corresponding concentrations for 24 hours. Cell viability was measured using the LIVE/DEAD Assay kit. Scale bars: 100 µm.
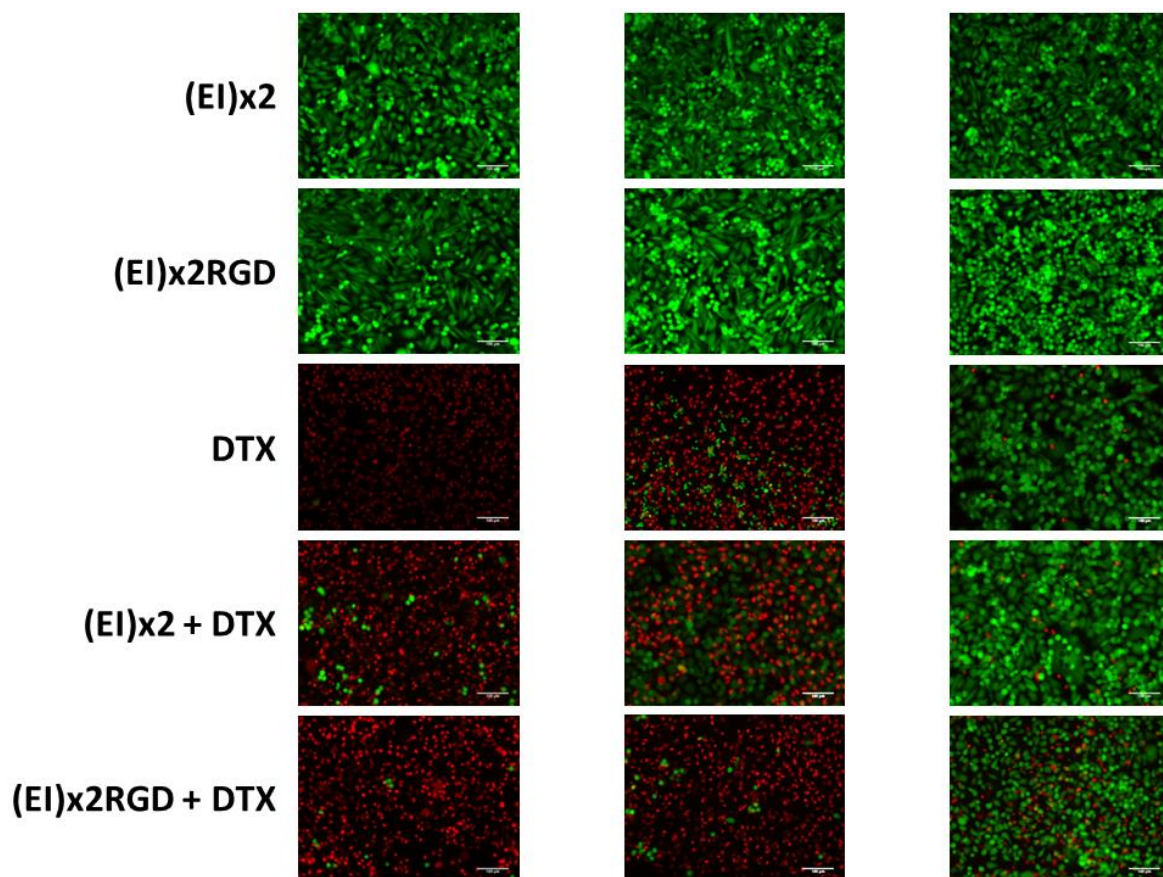
Figure S98. Representative fluorescence microscopy images for MDA-MB-231 cells after incubation with free DTX at three concentrations [0.1 (right column), 1 (middle column) and 10 µM (left column)] or encapsulated DTX within ELR nanoparticles at the corresponding concentrations for 24 hours. Cell viability was measured using the LIVE/DEAD Assay kit. Scale bars: 100 µm.